Article

Cell Reports

Functional Principles of Posterior Septal Inputs to the Medial Habenula

Graphical Abstract

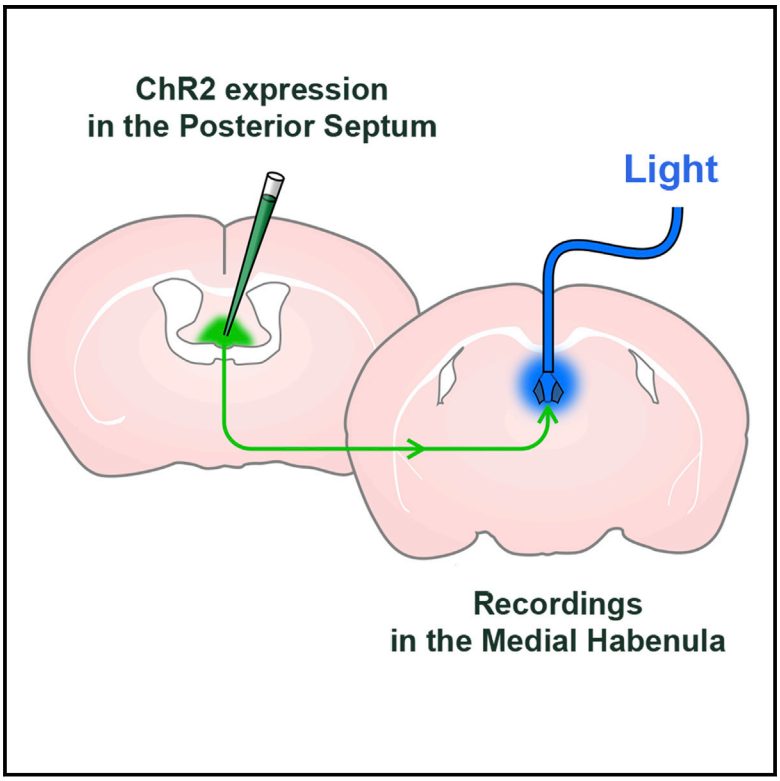

Highlights

- Medial habenular (MHb) neurons receive sparse inputs from the posterior septum (PS)
- PS afferents to the MHb function in a purely glutamatergic mode
- Excitatory ionotropic and inhibitory metabotropic receptors convey PS inputs in the MHb
- PS activation in the MHb increases locomotion and induces anxiolysis

Authors

Yo Otsu, Salvatore Lecca, Katarzyna Pietrajtis, ..., Caroline Mailhes-Hamon, Manuel Mameli, Marco Alberto Diana

Correspondence

marco.diana@upmc.fr

In Brief

The medial habenula (MHb) contributes to aversive state expression by linking forebrain areas to midbrain monoaminergic centers. Here, Otsu et al. provide a comprehensive characterization, from synaptic physiology to behavioral outcomes, of its glutamatergic afferents from the posterior septum, suggesting that septal stimulation in the MHb promotes locomotion and anxiolysis.

Otsu et al., 2018, Cell Reports *22*, 693–705
January 16, 2018
https://doi.org/10.1016/j.celrep.2017.12.064

CellPress

Cell Reports
Article

Functional Principles of Posterior Septal Inputs to the Medial Habenula

Yo Otsu,[1,3] Salvatore Lecca,[2,4] Katarzyna Pietrajtis,[1,7] Charly Vincent Rousseau,[1,5] Païkan Marcaggi,[1,6] Guillaume Pierre Dugué,[1] Caroline Mailhes-Hamon,[1] Manuel Mameli,[2,4] and Marco Alberto Diana[1,7,8,*]
[1]Institut de Biologie de l'École Normale Supérieure, INSERM U1024, CNRS UMR8197, École Normale Supérieure, PSL Research University, Paris, France
[2]Institut du Fer à Moulin, INSERM-UPMC UMR-S 839, Paris, France
[3]Present address: Institut du Fer à Moulin, INSERM-UPMC UMR-S 839, Paris, France
[4]Present address: Department of Fundamental Neuroscience, University of Lausanne, Lausanne, Switzerland
[5]Present address: Sainsbury Wellcome Centre for Neural Circuits and Behaviour, University College London, London W1T 4JG, UK
[6]Present address: INMED/INSERM U901, Parc scientifique de Luminy, 163 route de Luminy, Marseille 13009, France
[7]Present address: Sorbonne Universités, UPMC Université Paris 06, INSERM, CNRS, Neurosciences Paris Seine-Institut de Biologie Paris Seine (NPS-IBPS), 75005 Paris, France
[8]Lead Contact
*Correspondence: marco.diana@upmc.fr
https://doi.org/10.1016/j.celrep.2017.12.064

SUMMARY

The medial habenula (MHb) is an epithalamic hub contributing to expression and extinction of aversive states by bridging forebrain areas and midbrain monoaminergic centers. Although contradictory information exists regarding their synaptic properties, the physiology of the excitatory inputs to the MHb from the posterior septum remains elusive. Here, combining optogenetics-based mapping with *ex vivo* and *in vivo* physiology, we examine the synaptic properties of posterior septal afferents to the MHb and how they influence behavior. We demonstrate that MHb cells receive sparse inputs producing purely glutamatergic responses via calcium-permeable α-amino-3-hydroxy-5-methyl-4-isoxazolepropionic acid (AMPA), heterotrimeric GluN2A-GluN2B-GluN1 N-methyl-D-aspartate (NMDA) receptors, and inhibitory group II metabotropic glutamate receptors. We describe the complex integration dynamics of these components by MHb cells. Finally, we combine *ex vivo* data with realistic afferent firing patterns recorded *in vivo* to demonstrate that efficient optogenetic septal stimulation in the MHb induces anxiolysis and promotes locomotion, contributing long-awaited evidence in favor of the importance of this septo-habenular pathway.

INTRODUCTION

The habenular complex is a phylogenetically old structure (Stephenson-Jones et al., 2012) involved in the development, maintenance, and extinction of aversive states (Hikosaka, 2010). The habenula links limbic forebrain areas with subcortical nuclei releasing modulatory neurotransmitters (Hikosaka, 2010). In particular, the neurons of its medial subdivision, the medial habenula (MHb), control the serotoninergic raphe nuclei via its mixed cholinergic/glutamatergic projections (Ren et al., 2011) to the interpeduncular nucleus (IPN) (Gardon et al., 2014; Herkenham and Nauta, 1979). The MHb-IPN pathway has recently been characterized in view of its possible involvement in aversive aspects of nicotine addiction and withdrawal (Hsu et al., 2013) and of fear-related aversive states (Soria-Gómez et al., 2015; Zhang et al., 2016). In contrast with this well identified downstream connectivity, very little is known about the physiology of the only upstream source of glutamatergic excitation to the MHb, the posterior septum (PS) (Herkenham and Nauta, 1977), composed of the septofimbrial (SFi) and triangular nuclei (triangular septum [TS]) impinging on the ventral subdivision of the MHb (vMHb), and of the bed nucleus of the anterior commissure contacting the dorsal MHb (dMHb) (Qin and Luo, 2009). Synaptically, early studies identified mixed purinergic and glutamatergic excitatory synaptic inputs to the MHb from the PS in the rat (Edwards et al., 1992), characterized by the complete absence of functional N-methyl-D-aspartate (NMDA) receptors and by the calcium impermeability of the α-amino-3-hydroxy-5-methyl-4-isoxazolepropionic acid (AMPA) receptors mediating the glutamatergic component (Robertson and Edwards, 1998). These data could not be confirmed (Hamann and Attwell, 1996) and have not been re-examined so far.

Behaviorally, irreversible deletion of these inputs has been found to modify mobility, anxiety, and fear responses in mice (Yamaguchi et al., 2013), indicating their contribution to locomotion and emotional states. However, no information is available concerning the behavioral outcome of real-time modulations of the activity of PS projections.

By combining a large spectrum of techniques ranging from immunohistochemistry to two-photon calcium imaging, optogenetics-based mapping, and *ex vivo* and *in vivo* physiology, we provide here a comprehensive analysis of septo-habenular synaptic properties and identify some of its physiological functions.

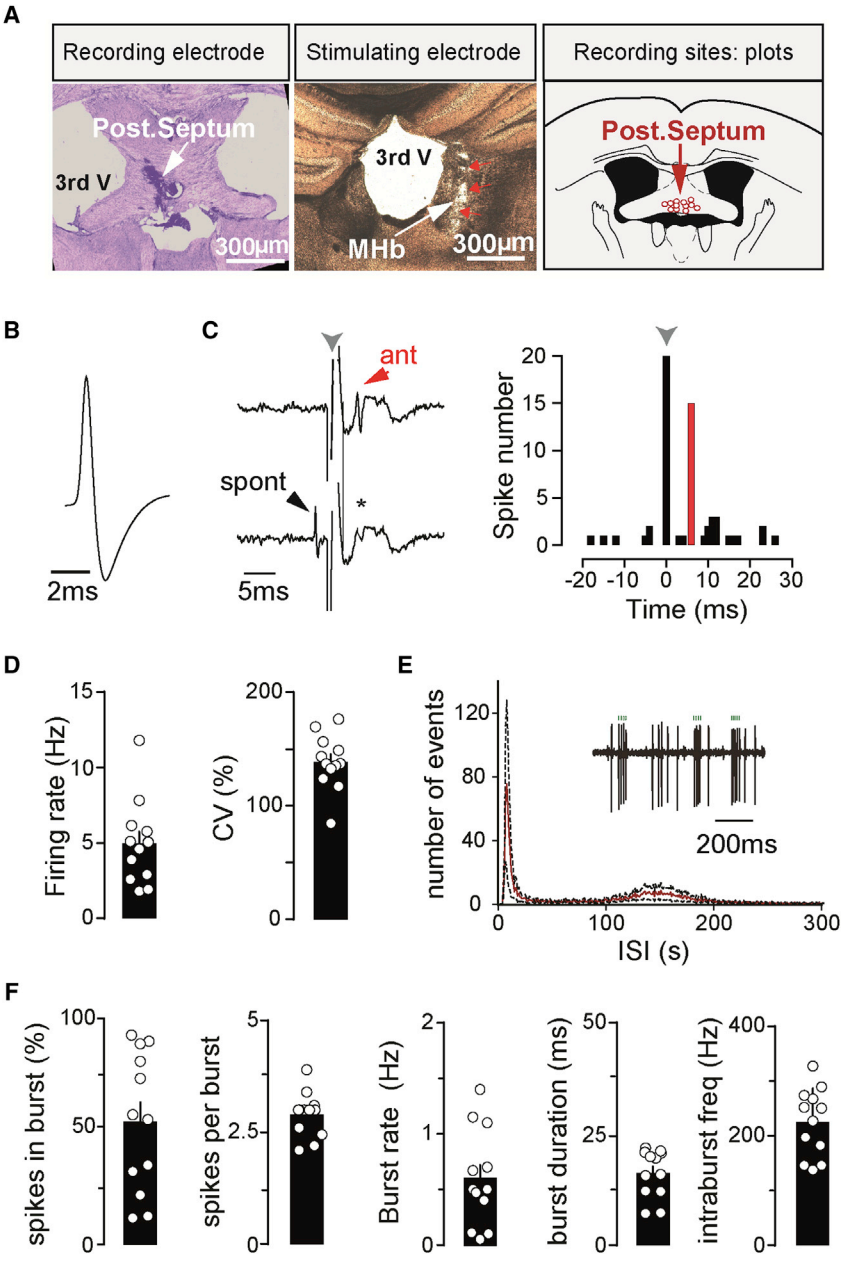

Figure 1. *In Vivo* Firing Features of MHb-Projecting Neurons in the PS

(A) The recording site of a PS cell is shown on the left. The electrode position was labeled with pontamine sky blue dye. Center: coronal section illustrating the stimulating electrode track (red arrows) within the MHb (white arrow). Right: the positions of all antidromically identified cells recorded in the PS are plotted schematically.

(B and D). The action potential waveform and pattern activity of a typical PS neuron is illustrated in (B). Plots and bar graphs reporting firing activity and coefficient of variation of the inter-spike interval (ISI) of all cells are depicted in (D).

(C) Typical traces showing the collision test allowing identification of MHb-projecting cells following antidromic stimulation. The left traces display an antidromically propagating spike (ant, top trace) following MHb stimulation (gray arrow) and its collision (*) when a spontaneous action potential (spont, bottom trace) preceded stimulation. On the right, the time histogram is shown for 20 stimulations of this same neuron, provided at t = 0 (1-ms bins, 0.5 Hz stimulation frequency). The gray arrow indicates stimulation onset. All antidromic spikes recorded occurred in correspondence with the red bin.

(E) Average ISI histogram of burst-displaying PS neurons. Data from all recorded cells are pooled, with the red line representing mean values and the black one depicting the SEM. A typical recording extract, showing spikes belonging to 3 distinct bursts (green dots), is shown in the inset.

(F) Graphs illustrating the main parameters of the bursting activity recorded in PS neurons.

Inspired by our recordings of the *in vivo* firing patterns of MHb-projecting PS neurons, we demonstrate that MHb cells are contacted by sparse fibers that operate exclusively in a glutamatergic mode via calcium-permeable AMPARs, heterotrimeric NMDARs, and inhibitory group II metabotropic glutamate receptors (mGluRIIs). Moreover, we describe the heterogeneity of MHb cell responses to optogenetic stimulation of PS fibers, examining the subtle interactions between ionotropic and metabotropic components in determining the temporal profile of firing changes. Finally, we devise a physiologically relevant optogenetic protocol to demonstrate that activation of the septohabenular projections increases mouse mobility and produces anxiolysis.

RESULTS

In Vivo Firing Pattern of MHb-Projecting Neurons in the PS

Our research aimed to provide a comprehensive portfolio of information concerning the synaptic physiology and behavioral role of PS inputs to the MHb. No information was available concerning neuronal activity in the PS before this study. A central initial step of our investigation thus consisted of the identification of *in vivo* PS firing patterns.

We performed single-unit recordings of the activity of MHb-projecting neurons in the PS of anesthetized mice (Figure 1). Cells were identified using high-frequency collision methods following antidromic stimulation (mean latency from stimulation, 6.2 ± 0.5 ms; n = 12 cells from 3 mice; Figure 1C) via a bipolar electrode placed in the MHb (Figure 1A; Glangetas et al., 2013). Iontophoretic application of pontamine sky blue allowed us to verify *post hoc* the position of recording sites (Figure 1A).

We examined several distinct parameters of neuronal activity (Figures 1D and 1F). Overall, the firing patterns of PS cells were irregular (Figures 1D and 1E), as illustrated by the coefficient of variation (CV) of the inter-spike interval (ISI; 138.5% ± 7.0%, n = 12). Moreover, most cells showed recurrent bursting

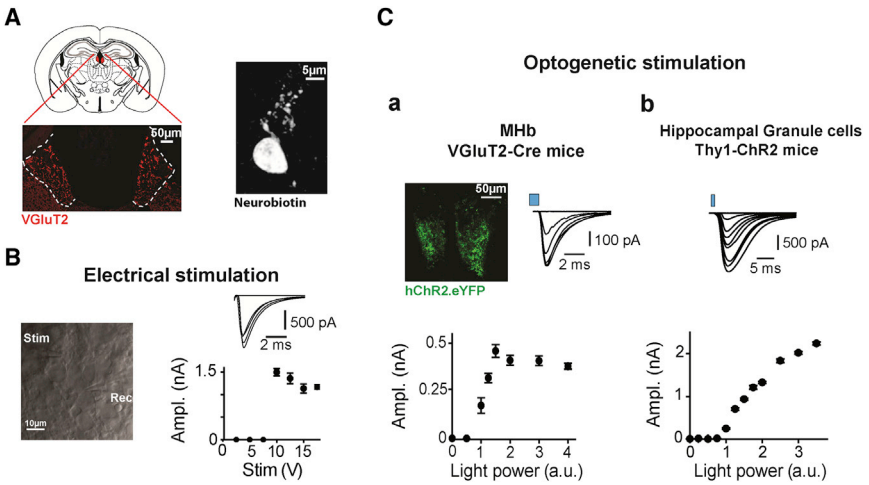

Figure 2. MHb Neurons Receive Sparse Afferents from the PS

(A) The MHb is highlighted in red in the schematic coronal brain section shown at top left. Bottom left: the MHb is illustrated at larger magnification in a slice in which VGluT2 was revealed immunohistochemically. VGluT2 marks the habenular glomeruli formed by glutamatergic terminals. On the right, the morphology of a typical MHb cell is shown. The neuron was filled with biocytin during whole-cell recording.

(B) Left: detail of the MHb from a slice, showing a whole-cell recording (Rec, right) and an extracellular stimulation electrode (Stim, left). EPSC amplitudes as a function of stimulation voltages are illustrated on the right for one neuron, with sample traces on top, showing the all-or-none nature of the evoked currents.

(C) The same type of experiment as in (B) but with an optogenetic approach. (a) YFP fluorescent signal in the vMHb (top left) following injection of a ChR2-YFP-expressing AAV in the PS of a VGluT2-Cre mouse. The dependence of liEPSC amplitudes on light power is illustrated for a typical experiment in the bottom graph, with corresponding raw traces (top right). Amplitudes showed discrete increasing steps. (b) The same stimulation approach was used in hippocampal granule cells of Thy1-ChR2 mice. In this case, the increase in liEPSC amplitudes with light was continuous, suggesting recruitment of a large number of afferent glutamatergic inputs. Both electrical and optogenetic responses were averaged over several repetitions (5 to 20) for each stimulation voltage and light power value, respectively. Error bars represent the SEM of the responses of a single cell to multiple trials at the stimulation intensities indicated on the x axes.

events lasting, on average, 16.2 ± 1.6 ms. In the recorded cells, 54.4% ± 8.9% of the total number of action potentials belonged to a burst, with the number of intra-burst spikes amounting to 2.9 ± 0.1 and occurring at an average intra-burst frequency of 224.8 ± 18.0 Hz (Figure 1F). Bursts per se appeared at an average frequency of 0.6 ± 0.1 Hz. The total firing frequency amounted to 5.0 ± 0.8 Hz.

These data provided relevant information for developing a proper *ex vivo* analysis of the synaptic properties of the septo-habenular pathway and for achieving consistent *in vivo* optogenetic activation.

Individual MHb Neurons Receive Sparse PS Excitatory Input

We then examined the synaptic properties of the PS afferents in coronal brain slices.

The MHb is located symmetrically on both sides of the third ventricle (Figure 2A). Neurons in the MHb display a typical morphology consisting of short, varicosity-rich dendrites originating from small oval somata (Figure 2A; Kim and Chang, 2005).

We recorded cells exclusively from the vMHb. Following pharmacological block of GABAergic responses, we stimulated incoming excitatory fibers with an extracellular pipette while voltage-clamping MHb neurons (Figure 2B). Plotting the amplitude of the induced currents as a function of stimulation intensity revealed all-or-none responses consistent with stimulation of individual fibers (Figure 2B, right; n = 7). We then complemented these observations with an optogenetic approach. VGluT2-Cre mice were injected in the PS with a double-floxed adeno-associated virus (AAV) virus expressing ChR2 (Supplemental Experimental Procedures). Based on immunohistochemical staining, VGluT2 indeed appeared as a ubiquitous presynaptic marker for MHb glutamatergic afferents (Figure 2A). These injections led to presynaptic expression of ChR2-yellow fluorescent protein (YFP) throughout the vMHb (Figure 2C, a), in the same septal afferents stimulated via the "classical" extracellular electrical method (see below for more details).

PS afferents were optogenetically stimulated. When plotted as a function of light power, the amplitude of the responses showed few step-like increases (3 to 4), probably indicating recruitment of a sparse number of afferent fibers (Figure 2C, a; n = 6), supporting the data obtained via extracellular stimulation. As a comparison, we examined the effects of optogenetic activation of glutamatergic fibers onto hippocampal granule cells of mice expressing ChR2 under the control of the promoter for Thy1 (Wang et al., 2007). Consistent with the fact that granule cells receive a large number of excitatory inputs from the perforant pathway (Amaral et al., 2007), increasing the light intensity induced an almost continuous increase in light-induced excitatory postsynaptic current (liEPSC) amplitude (Figure 2C, b; n = 7). Importantly, both in the hippocampus and in the MHb, liEPSCs were completely blocked by tetrodotoxin (TTX) (500 nM), to 3.0% ± 1.8% (n = 5, p = 0.01) and to 3.5% ± 2.9% (n = 7, p = 0.001) of the control, respectively. These data suggest that the increases in liEPSC amplitudes with light power in the hippocampus likely originated from fiber recruitment, indirectly validating our experimental approach in the MHb.

In conclusion, these experiments demonstrate that MHb neurons receive sparse inputs from excitatory axonal afferents originating in the PS.

Excitatory Inputs to MHb Neurons Are Purely Glutamatergic

Early studies reported that PS inputs showed a mixed glutamatergic/purinergic nature without functional NMDA currents (Edwards et al., 1992; Robertson and Edwards, 1998). We re-examined this issue. We found that inward currents issued from single electrical stimulations (eEPSCs) had a conventional

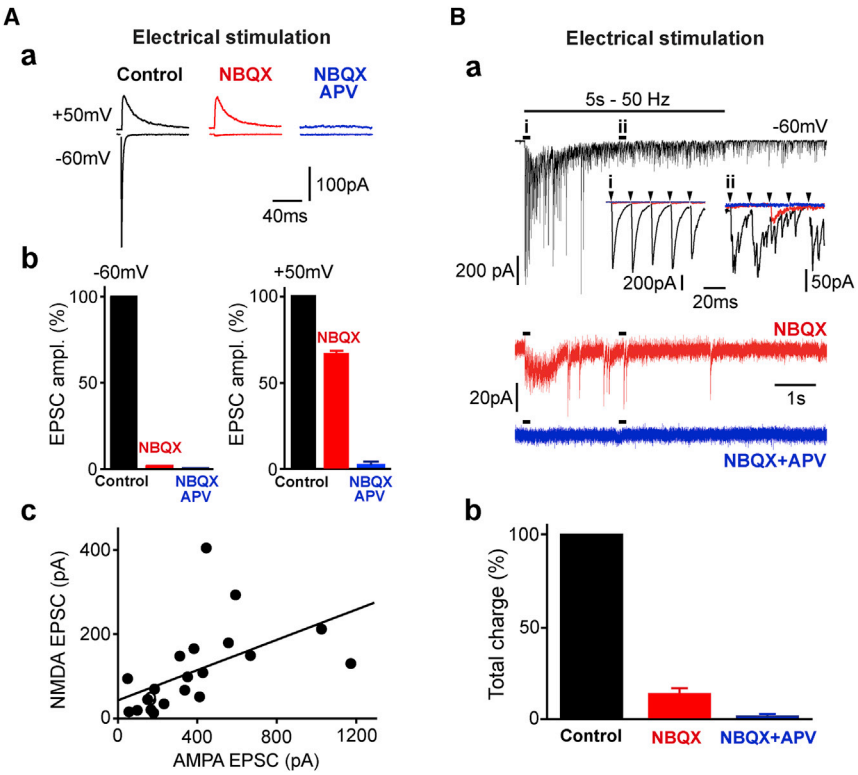

Figure 3. Posterior Septal Inputs to the MHb Are Purely Glutamatergic

(A). EPSCs show typical AMPA/NMDA profiles, with slower decay kinetics at +50 mV (top black traces) than at −60 mV (lower black traces) (a). Evoked responses were completely blocked following application of NBQX (red traces) and co-application of NBQX and APV (blue, right; b). The NMDA/AMPA amplitude ratio was correlated, although large variability in absolute values was observed between cells (c).

(B) Co-application of NBQX (alone in red traces) and APV (blue) completely blocked responses evoked by high-frequency trains (50 Hz for 5 s; a). Notice the rapid fatigue developing during the train, with transmission rapidly desynchronizing with respect to stimulation pulses (i and ii in a). The total charge transferred during trains is illustrated in (b), in control (black bar), after NBQX (red), and NBQX plus APV (red).

The data shown in this figure were obtained using extracellular stimulation. Stimulation artifacts were digitally removed for clarity. Pooled data are represented as mean ± SEM.

AMPA/NMDA glutamatergic profile (Figure 3A). The excitatory evoked postsynaptic current (eEPSC) average amplitudes were 369.3 ± 61.2 pA and 141.1 ± 21.0 pA at recording potentials of −60 mV and +50 mV (n = 23), respectively, with faster decay time constants at −60 mV (1.6 ± 0.1 ms) than at +50 mV (21.6 ± 4.4 ms, $p < 0.001$, n = 23; Figure 3A, a). The α-amino-3-hydroxy-5-methyl-4-isoxazolepropionic acid receptor (AMPAR) antagonist 2,3-dihydroxy-6-nitro-7-sulfamoyl-benzo[f]quinoxaline-2,3-dione (NBQX) (10 μM) almost completely abolished transmission at the hyperpolarized potential, to 4.4% ± 0.9% of the control ($p < 0.001$, n = 21), whereas it led to partial reduction of eEPSCs at the positive potential, to 72.4% ± 4.4% of the control ($p < 0.001$, n = 23). Co-application of the NMDAR antagonist (2R)-amino-5-phosphonopentanoate (APV) (50–100 μM) completely inhibited the remaining responses at both voltages, to 1.7% ± 0.7% (−60 mV, p = 0.004, n = 9) and 3.6% ± 0.6% of the control (+50 mV, p = 0.002, n = 10), demonstrating that single electric stimulations induced purely glutamatergic currents under our recording conditions (Figure 3A, b). Interestingly, the amplitudes of the AMPA and NMDA components showed great variability between cells (range, 50–1 200 pA; Figure 3A, c), although the NMDA/AMPA ratio was stable throughout the population tested (0.37 ± 0.08, p = 0.53, n = 23).

Mixed neurotransmission can be induced by stimulation trains (Ren et al., 2011). We thus examined the pharmacological profile of PS transmission during high-frequency trains (5 s, 50 Hz; Figure 3B). Repeated stimulations revealed 2 major properties of septo-habenular connections: asynchronous release developed rapidly in parallel with a powerful synaptic fatigue that reduced the total charge transferred in the last stimulation second to 32.4% ± 13.3% (4%–70%) of the corresponding value obtained during the first second (Figure 3B, a; p = 0.03, n = 5).

Stimulation trains still induced purely glutamatergic currents. At −60 mV, NBQX reduced the total charge transferred during the trains to 13.9% ± 3.0% of the control (Figure 3B, b; p = 0.03, n = 5). The remaining component was completely blocked by co-application of APV, to 1.6% ± 1.3% (p = 0.03, n = 5).

In conclusion, under our recording conditions, we could find no evidence for mixed ionotropic neurotransmission at PS-MHb inputs, which appear to operate in a purely glutamatergic mode.

AMPA Currents Are Mediated by Calcium-Permeable Receptors

AMPA transmission has been reported to be mediated by calcium-impermeable receptors in the MHb (Robertson et al., 1999). Consistently, our immunohistochemical data showed expression of both GluA1 and GluA2 AMPAR subunits in the MHb (Figure 4A). The insertion of GluA2 into AMPARs leads to both calcium impermeability and linearity of the IV curves of the currents. Surprisingly, examination of the electrically evoked AMPA currents (Figure 4B) revealed that synaptic currents displayed high rectification indexes (4.8 ± 0.3, n = 23), calculated as the ratio between AMPA EPSC amplitudes at −60 mV and at +50 mV. In comparison, perfect linearity of the current voltage (IV) curves of calcium-impermeable receptors would provide a theoretical rectification index of 1.75. Furthermore, the amplitude of AMPA EPSCs was rapidly and potently reduced, to

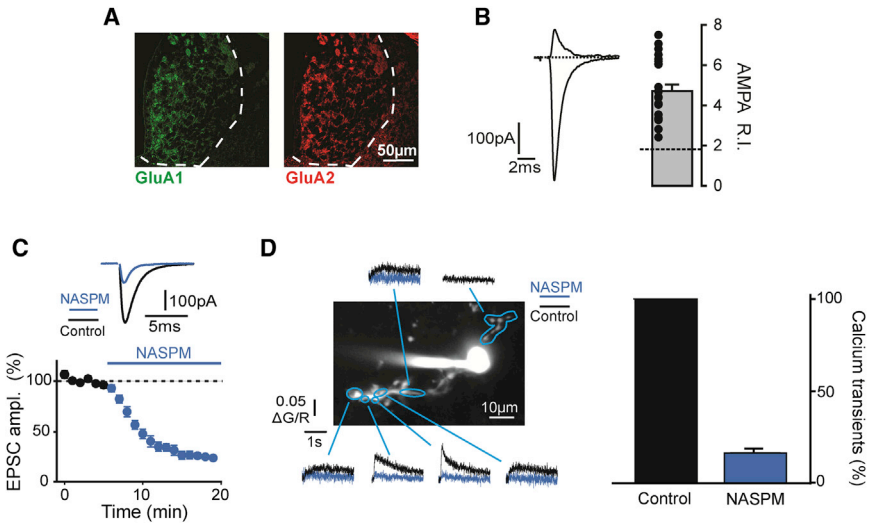

Figure 4. Calcium-Permeable AMPARs Mediate Glutamatergic Responses at Septo-habenular Inputs

(A and B) Immunohistochemical data demonstrated the presence of both GluA1 and GluA2 AMPAR subunits in the MHb (A). Nevertheless, electrically evoked AMPAR responses showed a large rectification index (B, right bar graph; the theoretical index [R.I.] for perfectly linear IV curves is shown by the dotted line, and values from each cell are depicted by points), suggesting the absence of GluA2 from postsynaptic densities under our recording conditions. Average EPSCs recorded at +50 mV (top) and −60mV (bottom) are illustrated for a typical cell on the left.

(C) Application of NASPM, a blocker of calcium-permeable AMPA conductances, rapidly and potently inhibited EPSCs.

(D) Two-photon calcium imaging experiments demonstrated that AMPAR activation triggers calcium elevations in MHb cell dendrites, which were blocked by NASPM. Quantification is depicted in the right bar graph. The time courses of the NASPM effect on calcium transients and EPSC amplitudes were similar (data not shown). Calcium increases were observed in several ROIs along dendrites (control, black; following NASPM, blue). However, rise times and amplitudes were largely heterogeneous, suggesting intracellular calcium diffusion from precise entry spots, probably identifying synaptic sites.

Pooled data are represented as mean ± SEM.

23.6% ± 2.2% of the control (p = 0.016, n = 7; Figure 4C) by the calcium-permeable AMPAR blocker 1-Naphthyl acetyl spermine (NASPM) (20–50 μM). We then performed two-photon calcium imaging experiments to examine the spatial distribution of the divalent permeability of AMPARs. We scanned the dendritic appendages of MHb cells loaded with Fluo-5F (500 μM), looking for calcium increases triggered by electrical stimulation of the incoming afferents. Evoked calcium transients could indeed be detected (Figure 4D; n = 9). Transients were normally limited to restricted areas of individual neurites and showed varying kinetics and amplitudes in regions of interest (ROIs) distributed along the responding processes. Application of NASPM (20–50 μM) decreased calcium signal amplitudes to 16.3% ± 2.6% of the control (Figure 4D; p = 0.016, n = 7), with a time course closely mirroring the temporal development of eEPSC inhibition.

Thus, in contrast to previous studies, our data establish the activation of calcium-permeable AMPARs by PS inputs to the MHb.

Subunit Composition of NMDARs in the MHb

We then examined the properties of the NMDA component. Immunohistochemical staining revealed robust expression of GluN1, GluN2A, and GluN2B subunits along the dorso-ventral MHb axis (Figure 5A).

Consistently, with the *in vivo* intra-burst frequencies of PS neurons (Figure 1), we used short (10 pulses), high-frequency (200 Hz) stimulation trains to obtain the IV curves of pharmacologically isolated NMDA currents (Figure 5B). The IV curves of NMDA currents showed the typical Mg^{2+}- and voltage-dependent rectification properties of NMDARs (Figure 5B; Paoletti et al., 2013), with their rectification increasing with extracellular Mg^{2+} concentrations. In Mg^{2+}-free solution, and at concentrations of 100 μM and 1.5 mM, total charge values recorded at −80 mV amounted to 92.9% ± 13.3% (n = 16), 21.6% ± 5.9% (n = 12), and 4.1% ± 1.1% (n = 10, p<0.001) of the value obtained at +50 mV (Figure 5B), respectively. The charge transferred by the train-evoked currents was completely blocked by APV, to 4.7% ± 1.3% of the control (n = 12 at +50 mV, p < 0.001).

We then analyzed the properties of individual NMDA currents in GluN2Ako mice (Figure 5C). The NMDA/AMPA current ratio was dramatically reduced in this mouse line with respect to wild-type (WT) littermates, from 17.4% ± 1.5% (n = 15) to 2.7% ± 0.4% (n = 12, p < 0.001; Figure 5C, a). This change was not associated with a significant difference in the AMPA EPSC amplitudes measured at −60 mV, which amounted to 588.6 ± 180.1 pA in the WT (n = 15) and to 756.0 ± 149.5 pA (n = 13, p = 0.3) in mutants. In contrast, the decay time course of NMDA EPSCs was dramatically slower than in the WT (Figure 5C, b), with time constants being 111.7 ± 33.9 ms in mutants (n = 7) and 22.9 ± 2.9 ms in control mice (n = 15, p < 0.001), consistent with the absence of the rapidly deactivating GluN2A subunits.

We finally tested pharmacological agents interfering specifically with GluN2A-, GluN2B-, and GluN2C/GluN2D-containing receptors: Zn^{2+} (300 nM), Ro25-6981 (1 μM), and (3-Chlorophenyl) [3,4-dihydro-6,7-dimethoxy-1-[(4-methoxyphenoxy) methyl]-2(1H)-isoquinolinyl]methanone (CIQ) (20 μM), respectively (Paoletti et al., 2013).

In WT mice, Zn^{2+} and Ro25-6981 had similar inhibitory effects on train-evoked NMDA responses (Figure 5D). Charge transfer was reduced to 62.8% ± 6.7% (n = 11, p = 0.001) and 63.9% ± 6.7% (n = 13, p < 0.001) of the pre-drug period, supporting the presence of both GluN2A and GluN2B subunits (Figure 5D, graph). As expected, in GluN2Ako mice, Zn^{2+} had no effect (100.3% ± 4.2% of the control, n = 5, p = 1.0), whereas Ro25-6981 inhibited the responses to a greater extent than in

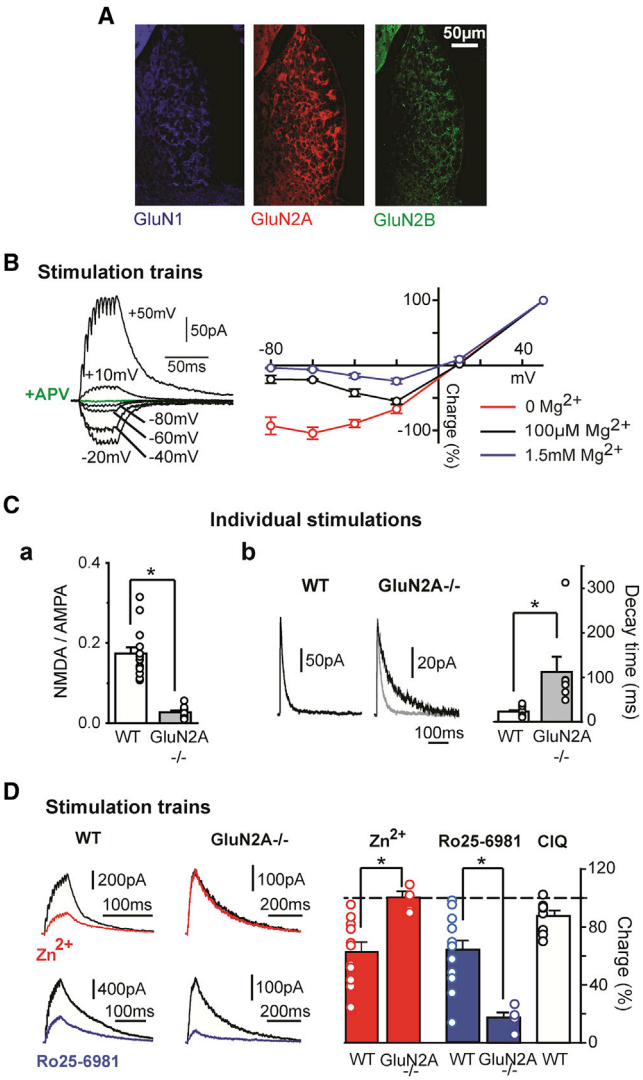

Figure 5. NMDARs Are Composed of GluN1-GluN2A-GluN2B Heterotrimers at PS Inputs to the MHb

(A) Immunohistochemistry revealed expression of GluN1, GluN2A, and GluN2B in the MHb.

(B) The IV curves of pharmacologically isolated NMDA EPSCs (right graph) showed larger rectification with increasing extracellular Mg^{2+} concentrations. Trains of 10 stimulations at 200 Hz were applied to trigger NMDA responses (the left traces were obtained at the Mg^{2+} concentration of 1.5 mM).

(C) NMDA EPSCs were strongly reduced in GluN2Ako mice, as illustrated by the NMDA/AMPA ratio (a), with dramatically slower decay times than in wild-type (WT) mice (b). Sample traces for one WT (left) and one GluN2Ako cell (right; the WT trace is superimposed in gray) are also shown.

(D) Pharmacological analysis of NMDA currents. Zn^{2+} (red) and Ro25-6981 (blue), specific blockers of GluN2A and GluN2B subunits, respectively, antagonized NMDA responses with similar efficacy in WT mice. Zn^{2+} had no detectable effects, whereas Ro25-6981 action was potentiated in GluN2AKO mice, suggesting that NMDARs are most likely formed by GluN1-GluN2B heterodimers when GluN2A is ablated genetically. CIQ, which specifically potentiates GluN2C- and/or GluN2D-containing receptors, had no significant effects on evoked responses in WT mice.

*$p < 0.05$; pooled data are represented as mean ± SEM.

WT mice (to 17.4% ± 3.4% of the control, n = 5, p = 0.03 with respect to pre-drug period; p = 0.003 with respect to the WT), suggesting that, in GluN2Ako mice, NMDARs are predominantly composed of GluN2B-GluN1 heterodimers (Figure 5D; Hatton and Paoletti, 2005). Finally, we examined the effect of CIQ, a drug specifically potentiating GluN2C/GluN2D-containing receptors. In our experiments, CIQ produced a small inhibition of NMDA responses to 87.6% ± 3.6% of the control (n = 9, p = 0.01; Figure 5D, graph), indicating a lack of GluN2C/GluN2D subunits in the MHb.

In conclusion, our experiments support the existence of conventional, heterotrimeric NMDARs containing GluN1-GluN2A-GluN2B in the MHb (Paoletti et al., 2013).

Ionotropic and Metabotropic Glutamate Receptors Differentially Regulate MHb Cell Firing

Both excitatory and inhibitory metabotropic receptors (mGluRs) can be activated by synaptic glutamate release, with effects on firing spanning several hundred milliseconds. We examined the possible presence of functional mGluRs in vMHb neurons by puffing agonists of group I, group II, and group III mGluRs on cells recorded in the loose cell-attached (LCA) configuration (Figure S1). Ventral MHb cells are indeed spontaneously active in slices (Görlich et al., 2013). We found that mGluRIIs are functionally expressed in virtually all cells, and that their activation potently inhibits firing via development of slow outward currents (Figure S1). In contrast, mGluRIIIs and mGluRIs are either not expressed or expressed at low levels in the vMHb respectively.

Besides ionotropic excitatory receptors, the glutamate released from PS inputs might thus also activate inhibitory mGluRIIs. We therefore examined the effect on MHb neuronal activity of optogenetically stimulated PS fibers. VGluT2-Cre mice were injected in the PS with a double-floxed ChR2-expressing AAV. The optogenetically stimulated fibers were most likely the same type of afferents activated electrically (Figure 6A). Indeed, liEPCSs were purely glutamatergic. In the whole cell configuration, their amplitude was completely blocked by co-application of NBQX and APV, to 1.3% ± 0.3% (n = 28, p = 0) and 3.1% ± 1.2% (Figure 6A, right graph; n = 11, p = 0.003) of the control at −60 mV and +50 mV. Furthermore, neither the AMPA rectification index (4.8 ± 0.6, n = 22, p = 0.4) nor the NMDA/AMPA ratio (Figure 6A; 36.0% ± 4.3%, n = 18, p = 0.5) were significantly different from the values obtained with electrical stimulation.

In the LCA configuration, we examined the changes in firing frequency upon optogenetic stimulation of PS afferents. We used 5-s-long trains at 20 Hz, a train pattern allowing reliable optogenetic stimulation over the short *ex vivo* recording times. We pooled MHb cells into three distinct groups according to the response patterns found.

The first group comprised MHb neurons in which ChR2 activation produced a dramatic increase in the firing rate during stimulation, to 774.5% ± 125.1% of the control (Figure 6B; n = 48, p < 0.001), followed by action potential inhibition in the 2 s after train end, to 30.0% ± 6.9% of the control (p < 0.001). We found that both phenomena were dependent on activation of ionotropic glutamate receptors. Co-application of NBQX and APV indeed eliminated the late inhibition of the firing rate,

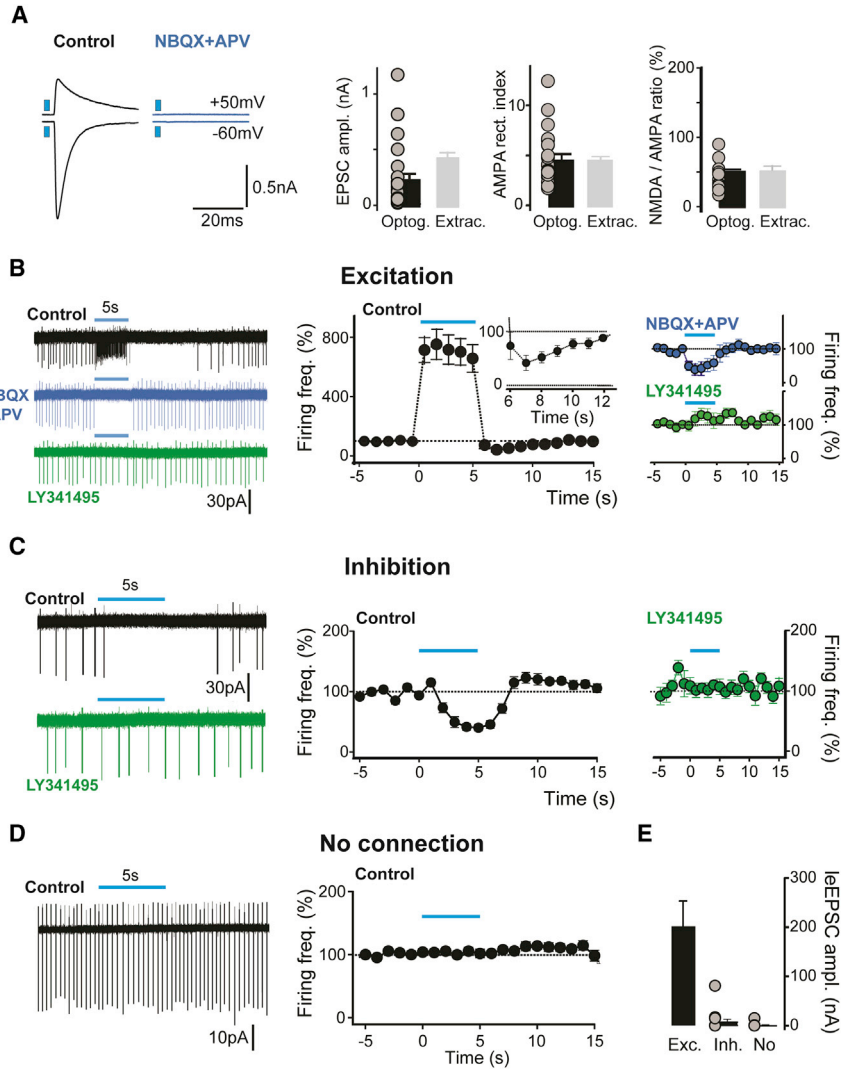

Figure 6. Integrative Properties of Septo-Habenular Afferent Activity by MHb Neurons

(A and B) Optogenetic stimulation of septal afferents in VGluT2-Cre mice injected with a ChR2-expressing AAV activated a similar groups of fibers as extracellular stimulation. The traces on the left illustrate a typical MHb neuron in which ChR2 activation produced synaptic responses mediated by AMPA and NMDA (clearly visible at +50 mV, top) receptors. The graphs in (A) show that EPSC average amplitudes (left), AMPA rectification indexes (center), and average NMDA/AMPA amplitude ratios (right) were statistically indistinguishable following either optogenetic (Optog., left bar; individual cells depicted as gray points) or extracellular electrical stimulation (Extrac., light gray bars; data already shown in previous figures). In the LCA recording configuration, a 5-s-long blue light stimulation train at 20 Hz distinguished 3 groups of neurons. In the first group (n = 48; B), a dramatic increase in spike rate during the train was followed by strong inhibition in the seconds following the stimulation end (detailed at larger magnification in the inset). Augmentation and post-train inhibition were both blocked by co-application of NBQX and APV, and were replaced by a significant decrease of firing, which was completely eliminated by bath application of the mGluRII antagonist LY341495 (right graphs).

(C) A group of cells (n = 53) is shown, where activation produced dramatic inhibition of the firing rate, which was mGluRII-dependent (right graph).

(D) In several cells (n = 41), ChR2 activation triggered no detectable change in firing.

(B–D) The traces on the left show a typical recording, whereas the time courses of firing changes for all analyzed cells are depicted in the right graphs. Color codes for traces and temporal graphs are black for control, blue for NBQX and APV co-application, and green for LY341495 in the bath either following NBQX and APV (B) or alone (C). Blue lines represent the 5-s-long stimulation trains.

(E) EPSC amplitudes recorded in the whole-cell configuration for a subset of cells in which light trains produced either excitation (Exc.; left bar), only inhibition (Inh.; center bar), or no effect (No; right bar).

Pooled data are represented as mean ± SEM.

which was 83.6% ± 19.0% of the pre-stimulation period after drug application (n = 11, p = 0.4). The early excitatory phase was instead replaced by a prominent inhibition, to 46.8% ± 8.8% of the control (n = 15, p = 0.01), which was mediated by mGluRII activation because it was canceled by subsequent application of the mGluRII antagonist LY341495 (1μM; spike rate during light trains, 112.7% ± 12.9%; n = 11; p = 0.6). A subset of this cell group was also recorded in the voltage clamp (VC) configuration. Here, optogenetic stimulation invariably produced AMPA and NMDA liEPSCs, showing the presence of a direct synaptic connection (see Figure 6E and also Figure 6A for average amplitudes and pharmacological profile; n = 28). The firing pattern in response to PS fiber activation was also examined in current clamp (CC) recordings (Figure S2). The results fully confirmed the findings of LCA recordings (Figure S2), further supporting the hypothesis that the inhibition of the firing rate following excitation was due to AMPAR/NMDAR-dependent activation of intrinsic conductances (Figure S2B) and not to activation of local inhibitory interneurons (which are not present in the MHb; Figure S4). These data thus demonstrate that AMPAR and NMDAR activation can entrain MHb cells firing very efficiently, prevailing over inhibitory metabotropic components.

In a second group of neurons, optogenetic stimulation trains decreased spike rates to 49.7% ± 3.9% of the control (Figure 6C; n = 53, p < 0.001). We found that this inhibition was due to mGluRII activation because LY341495 prevented the decrease in firing, which amounted to 107.7% ± 7.7% of the control (n = 11, p = 0.003). Interestingly, the glutamate transporter blocker DL-threo-β-Benzyloxyaspartic acid (DL-TBOA) (100 μM) potentiated the spike rate inhibition of this group of cells, with frequencies reduced to 65.6% ± 6.2% in the control

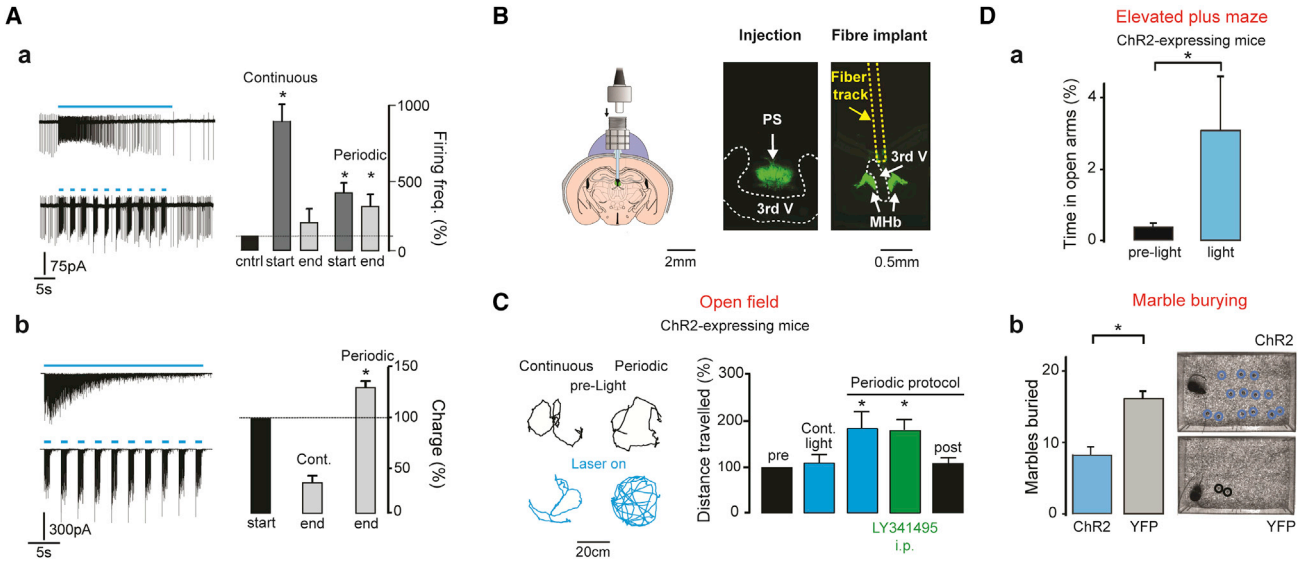

Figure 7. Synaptically Efficient Optogenetic Stimulation of the Septo-habenular Pathway Induces Anxiolysis and Increases Mouse Mobility

(A) Continuous optogenetic stimulation (30 s, 20 Hz) rapidly lost efficiency at increasing firing of MHb cells in LCA recordings. The response of a typical neuron is illustrated (top left; quantification in the right graph). In contrast, periodic laser-on (1 s)/laser-off (2 s) trains quantitatively maintained their effect over long periods (bottom traces and bar graph). Firing was quantified in the first (start) and last (end) 4 s of stimulation as percentage of control spike rate. (b) In the whole-cell configuration, dramatic synaptic fatigue developed rapidly during continuous trains but not during periodic stimulation, consistent with the results shown in (a). The charge transferred at stimulation end was quantified as a percentage of the charge obtained at train onset.

(B) For *in vivo* optogenetic experiments, injected mice (see center for fluorescence at the PS injection site of one mouse) were implanted with a fiber optic just above the MHb, as shown schematically on the left and for one animal on the right (the fiber track is highlighted in yellow).

(C) Intermittent stimulation in freely moving, ChR2-expressing VGluT2-Cre mice robustly increased locomotion. In contrast, continuous trains did not produce significant changes in the total distance traveled (quantified in the right bar graph). Mouse position in the open-field arena in time is shown for one animal before (left black traces, corresponding to 1-min-long period) and during stimulation (bottom, blue) for continuous (left) and periodic (right) trains. The effect on locomotion of the intermittent protocol was also maintained following intraperitoneal (i.p.) injection of LY341495 (quantifications shown in the right bar graph). Light trains produced no significant change in locomotor activity in VGluT2-Cre mice expressing only eYFP at PS inputs (data not shown).

(D) PS input activation in the MHb is anxiolytic. (a) ChR2-expressing mice spent more time in the open arms of an EPM during optogenetic stimulation (blue bar) than in the pre-light period (black). (b) ChR2-YFP expressing mice buried significantly fewer marbles than animals expressing only YFP (quantified in the left graph). The images illustrate the unburied marbles for 2 mice.

Pooled data are represented as mean ± SEM.

period and to 38.8% ± 8.0% during drug application (n = 11, p = 0.004; Figure S3), suggesting an extrasynaptic localization of mGluRIIs and the possibility of spillover-mediated heterosynaptic inhibition in MHb glomeruli (Kim and Chang, 2005). Whole-cell VC analysis revealed that light pulses induced liEPSCs only in a small percentage of cells (Figure 6E; average amplitude, 8.2 ± 5.8 pA, with only 3 of the 14 neurons showing detectable liEPSCs), whereas stimulation trains consistently activated small but detectable mGluRII-dependent outward currents at a recording potential of −45 mV (Figure S2C). Thus, in most cases, AMPARs and NMDARs were either not activated or activated only weakly by glutamate release, the dominant effect being inhibitory mGluRII activation.

We finally found MHb neurons in which optogenetic stimulation produced no effect (Figure 6D; 103.6% ± 3.0% of the control; basal firing rate range, 0.5–6.7 Hz; n = 41; p = 0.9). As expected, VC recordings revealed no detectable current (Figure 6E; liEPSC amplitude, 0.9 ± 0.8 pA; n = 19). In this case, inefficient infection of PS cells probably led to the lack of ChR2 expression in the presynaptic afferent(s).

In conclusion, we demonstrated that optogenetic activation of PS inputs produces complex bi-phasic excitatory/inhibitory responses in MHb cells. In the Discussion, we describe several diverse factors possibly concurring to shape the spatiotemporal profile of the responses.

In Vivo Optogenetic Stimulation of PS Inputs to the MHb

We then investigated the efficacy of distinct stimulation patterns of PS inputs. The fatigue observed *ex vivo* with continuous stimulations (Figure 2B, a) suggested that the bursting firing patterns of PS neurons recorded *in vivo* (Figure 1) may be imperative for maintaining synaptic efficacy over long activity periods.

We first tested continuous optogenetic trains with a duration (30 s) and frequency (20 Hz) commonly used under *in vivo* conditions. We examined the reliability of this protocol in modifying neuronal activity. Only neurons showing excitation/inhibition cycles were examined. In both LCA (Figure 7A, a) and VC (Figure 7A, b) recordings, we found that these stimulation trains rapidly lost much of their efficacy in increasing the firing rate and transferring the excitatory charge, respectively. In LCA recordings, the firing rate during the first 4 stimulation seconds was 888.2% ± 279.1% of the control, whereas it was not significantly different from the pre-stimulation period in the last 4 s (192.1% ± 95.4%, n = 15, p = 0.98; Figure 7A, a, top trace).

Similarly, in VC recordings, the charge transferred in the last seconds of stimulation was 42.8% ± 11.1% of the charge transferred at train onset (n = 22, p = 0.0004; Figure 7A, b, top trace). Importantly, NBQX completely blocked all charge transfer at −60 mV (to 0.3% ± 0.2% of the control trains, n = 9, p < 0.0001; data not shown), further confirming the purely glutamatergic nature of these synapses.

Continuous optogenetic stimulation, thus, does not represent a valuable strategy for proper activation of PS inputs to the MHb. Our *in vivo* data on PS firing led us to apply brief light-on periods (20 Hz, 1 s) alternated with light-off periods (2 s) over a total duration of 30 s (Figure 7A). Optogenetic stimulation at 20 Hz represents an upper limit for ChR2 stimulation in trains. By using 1-s-long trains, we compensated for the fact that this value is 10-fold lower than the average intra-burst frequency (Figure 1F).

In both LCA and VC recordings, this protocol was very efficient over long stimulation periods. The firing rate at intermittent stimulation onset was smaller than for continuous trains (399.8% ± 68.9%, n = 16, p = 0.006 with respect to continuous trains; Figure 7A, a, bottom trace). Nevertheless, in the last 4 s, periodic stimulation still significantly increased the firing rates (305.2% ± 84.0%, n = 16, p = 0.003 with respect to the pre-stimulation in LCA, p = 0.006 versus the same time window of continuous trains; Figure 7A, a).

In VC recordings, the charge transferred at train end was not different from the onset and, in percentage, greater than for continuous trains (132.3% ± 13.5%, n = 22, p = 0.3 and p = 0.0001 versus the first 4 stimulation seconds and versus the corresponding time window for continuous stimulation, respectively; Figure 7A, b). The intermittent protocol allowed us to examine how prolonged *in vivo* activation of PS inputs to the MHb may affect behavior.

Septo-habenular Glutamatergic Inputs Stimulate Locomotion and Produce Anxiolysis

VGluT2-Cre mice injected with either a double-floxed ChR2- or a YFP-expressing virus were implanted with an optic fiber cannula just above the third ventricle (Figure 7B).

Mouse locomotion in an open-field arena was examined before, during, and after laser stimulation trains both with the continuous and with the periodic laser-on/laser-off 20-Hz protocol used before (Figure 7C). We examined locomotion because the MHb contributes to rodent mobility (Yamaguchi et al., 2013). We found that continuous stimulation of ChR2-expressing mice did not alter locomotion (110.0% ± 17.4%, n = 11, p = 0.9 versus the pre-light control period). In contrast, intermittent stimulation led to a significant augmentation of the total distance traveled (200.0% ± 37.3%, p = 0.02 and p = 0.04 with respect to the control period and to continuous stimulation, n = 11; Figure 7C). After the stimulation protocol was terminated, mouse mobility returned to control levels (110.6% ± 12.1%, p = 0.6; Figure 7C).

Locomotion remained unaltered in mice injected with a control virus, the distance traveled amounting to 123.6% ± 15.5% (n = 8, p = 0.4; data not shown) of the pre-stimulation period for the continuous pattern and to 106.3% ± 5.5% (n = 8, p = 0.2; data not shown) for the intermittent one.

Finally, we tested whether the effect of *in vivo* stimulation could be attributed either to the activation of ionotropic (the cell group shown in Figure 6B) or of mGluRII glutamate receptors (Figure 6C). The intermittent protocol was applied to mice that were previously injected intraperitoneally with the blood-brain barrier-permeable mGluRII antagonist LY341495 (1–4 mg/kg). We found that optogenetic stimulation still increased locomotion in mice, to 174.9% ± 23.8% of the control (n = 10, p = 0.8 versus intermittent stimulation under control conditions; Figure 7C, green bar in the graph), suggesting that the neurons responsible for this behavioral response are the ones excited by AMPAR and NMDAR activation (Figure 6B).

We then examined the effect of PS inputs on anxiety levels (Yamaguchi et al., 2013). First, no difference was detected in the percentage of time spent by ChR2-expressing mice in the center of the open field during intermittent stimulation patterns (35.7% ± 7.4% before light onset versus 35.4% ± 4.1% during stimulation, p = 0.9; data not shown). In contrast, in the elevated plus maze (EPM) test, ChR2-injected mice significantly spent more time in the open arms during stimulation with respect to preceding control periods (3.3% ± 1.5% versus 0.3% ± 0.1%, p < 0.05, n = 11; Figure 7D, a). The EPM results may be affected by the increased locomotion of the mice. We therefore also performed the marble burying (MB) test. In this test, ChR2-expressing mice buried significantly fewer marbles during light stimulation than YFP-expressing animals (9.4 ± 2.0 with n = 10 versus 16.1 ± 1.8 with n = 8, p = 0.03; Figure 7D, b), confirming the anxiolytic effect of intermittent, physiology-like stimulation of PS inputs to the MHb.

In conclusion, these results illustrate the validity of our intermittent stimulation pattern for eliciting optogenetic responses. Furthermore, they demonstrate that PS activation can control mobility and anxiety states.

DISCUSSION

Our work represents a comprehensive characterization, from synaptic components to behavioral outcomes, of the septo-habenular glutamatergic afferent system. These data fill a long-standing information gap. On one side, the role of the PS as a source of glutamatergic inputs to the MHb has indeed been known for decades in morphological terms (Herkenham and Nauta, 1977). In contrast, much less functional information was available before this study, certainly because of the sparse innervation of MHb cells (Figure 2) and of the laboriousness in activating these inputs in slice preparations before the advent of optogenetics.

PS Afferents to the MHb Are Purely Glutamatergic

Early studies dating back more than 20 years suggested that PS inputs co-released glutamate and ATP (Edwards et al., 1992; Robertson and Edwards, 1998). The glutamatergic component was reported to be mediated by calcium-impermeable AMPARs without concomitant NMDAR activation. Our data depict a strikingly contrasting portrait. We indeed provide evidence that these inputs are purely glutamatergic, with responses produced by activation of both calcium-permeable AMPARs and GluN2A-GluN2B-GluN1 heterotrimeric NMDARs (Figures 4 and 5).

Differences exist in the experimental conditions, possibly explaining these contradictions, mainly the use of young rats (Edwards et al., 1992) versus adult mice (here) and the ambient versus physiology-like temperatures (here) at which data were collected. Moreover, the purinergic component was generally triggered by higher stimulation intensities than the glutamatergic one (Robertson and Edwards, 1998), with extracellular applied voltages that can lead to transient electroporation of cellular membranes (Hamann and Attwell, 1996).

One physiological implication of such a variety of calcium sources in MHb neurons could obviously be synaptic plasticity. Among other roles, the MHb may be a central region for mediating nicotine and opioid addiction-related aversive states (Fowler et al., 2011; Frahm et al., 2011; Gardon et al., 2014). Synaptic plasticity may thus be central for putting in place the circuital modifications associated with repeated drug use. It will therefore be important to investigate whether PS inputs to the MHb show forms of long-term synaptic plasticity and their possible behavioral implications.

MHb Integration Properties of PS Inputs at the Cellular and Circuital Levels

Our data illustrate a rather complex pattern of integration properties of the sparse PS inputs by MHb cells. We have shown that activation of the ionotropic components of glutamatergic EPSCs, when present, is extremely efficient in driving MHb neurons (Figures 6 and 7). In contrast, if AMPA and NMDA components are absent, then the net stimulation effect often appears to be powerful activity inhibition. The activation of mGluRIIs and the consequent decrease in firing may be explained by two configurations: either postsynaptic densities only express metabotropic receptors, or mGluRIIs located at the periphery of the active zones sense glutamate diffusing from heterosynaptic sites. We are in favor of the latter hypothesis. First, blocking glutamate transporters potently increased the inhibitory effect of metabotropic activation on firing (Figure S3), suggesting a peripheral position of the receptors with respect to glutamate release sites. Furthermore, PS afferents appear to form glomerular specializations in the MHb (Kim and Chang, 2005), where dendrites from several distinct cells converge, providing an ideally ''closed'' environment for efficient glutamate spillover.

On a more circuitry-centered point of view, inhibition via mGluRIIs may be considered as a lateral inhibition-like synaptic phenomenon. Individual PS fibers might indeed lead to strong activation of their corresponding postsynaptic targets and to inhibition of close-by, not directly contacted MHb cells, increasing the contrast of the incoming information. It is relevant to underline that, inside the classically identified ventral and dorsal MHb, several molecular markers distinguish further sub-regions (Aizawa et al., 2012; Görlich et al., 2013; Gardon et al., 2014) and that two specific areas in the zebrafish equivalent of the mammal vMHb have been recently found to have opposite roles in social contrast resolution processes (Chou et al., 2016). The equivalence of circuital organization between zebrafish and mouse still remains uncertain. However, this mGluRII-mediated inhibitory mechanism might contribute to refining the spatial profile of the activated habenular sub-regions, optimizing information transfer via this epithalamic relay.

General Remarks on MHb Excitatory Inputs: Behavioral Consequences

In this study, we illustrated an efficient optogenetic protocol for *in vivo* PS fiber stimulation in the MHb. Our findings suggest that the PS controls locomotion (similar to Yamaguchi et al., 2013) and induces anxiolysis. The latter result is surprising in view of the general assumption that MHb activation is coupled to enhancement of negatively valued states and of the finding that deleting PS inputs decreases anxiety (Yamaguchi et al., 2013). Importantly, though, increased MHb excitability and/or output efficiency can also contribute to relieving negative states, for example, during fear conditioning (Soria-Gómez et al., 2015; Zhang et al., 2016).

Our results may also be explained by the emerging complexity of afferent synaptic excitation to the MHb. Defying expectations, several groups have indeed reported that GABAergic afferences increase, rather than decrease, neuronal firing in the MHb (Kim and Chung, 2007; Choi et al., 2016; Koppensteiner et al., 2016). Similarly to glutamatergic fibers, GABAergic axons impinging onto MHb cells originate in septal nuclei (Qin and Luo, 2009). Morphologically, GABAergic fibers form classical small terminals on postsynaptic dendrites, externally with respect to glutamatergic glomeruli (M.A.D., unpublished data). Thus, GABAergic terminals produce clearly distinct structures in comparison with glutamatergic ones, and they may therefore efficiently convey different activity patterns onto MHb cells. It is tempting to speculate that, downstream in the raphe nuclei via the IPN relay, this heterogeneity of incoming excitation to MHb cells may produce divergent spatiotemporal patterns of serotonin release throughout the brain and, thus, distinct behavioral outcomes. It will be important in the future to understand how the excitatory role of GABAergic synapses can be reconciled with that of the glutamatergic inputs described here.

In conclusion, by establishing the physiological contour of septo-habenular glutamatergic function, we provide here long-awaited foundations for further exploration of the role of the MHb in brain physiology.

EXPERIMENTAL PROCEDURES

All procedures involving experimental animals were performed in accordance with Directive 2010/63/EU, the guidelines of the French Agriculture and Forestry Ministry for handling animals, and local ethics committee guidelines.

Ex Vivo Electrophysiology

Adult mice (≥ 3 months old) were used for this study. Coronal slices (300 μm) were prepared, and recordings were performed at 30°C–34°C as described previously (Giber et al., 2015) from both C57/B6 mice, GluN2KO mice and their control littermates, VGluT2-Cre mice, and, finally, from Thy1-ChR2 mice (line 18; Wang et al., 2007).

All recordings were performed in a bicarbonate buffered solution (BBS) containing the following (mM): 116 NaCl, 2.5 KCl, 1.25 NaH_2PO_4, 26 $NaHCO_3$, 30 glucose, 2 $CaCl_2$, 1.5 $MgCl_2$, and 5×10^{-5} minocycline (bubbled with 95% O_2, 5% CO_2). We recorded neurons located exclusively in the vMHb. For whole-cell (WC) recordings, patch pipettes (resistance, 2.5–4 megaohms [MΩ]) were filled with an intracellular solution containing 150 mM $CsMeSO_3$, 10 mM tetraethylammonium chloride (TEA·Cl), 1 mM $CaCl_2$, 4.6 mM $MgCl_2$, 10 mM 4-(2-hydroxyethyl)-1-piperazineethanesulfonic acid (HEPES), 10 mM K_2-creatine phosphate, 0.5 mM EGTA, 4 mM Na_2-ATP, 0.4 mM Na_2-GTP,

0.1 mM spermine, and 2 mM QX-314, pH 7.35 with CsOH (~300 mOsm), sometimes supplemented with a morphological dye (5 μM Alexa 488, Invitrogen) to check cell morphology. For CC recordings (Figure S2) and experiments examining (2S,2'R,3'R)-2-(2',3'-Dicarboxycyclopropyl)glycine (DCG-IV)-induced currents in whole cell (Figure S1), the intracellular solution contained 150 mM K-Gluconate, 4 mM NaCl, 10 mM HEPES, 10 mM K_2-phosphocreatine, 0.1 mM EGTA, 6 mM Mg_2ATP, and 0.4 mM NaGTP. LCA (seal resistance, 10–20 MΩ) recordings were performed at a holding potential of −60 mV, with pipettes filled with an HEPES-buffered solution (HBS) containing 130 mM NaCl, 2.5 mM KCl, 1.25 mM NaH_2PO_4, 30 mM glucose, 2 mM $CaCl_2$, 1.5 mM $MgCl_2$, and 10 mM HEPES, pH 7.35 with NaOH (~300 mOsm). Currents were filtered at 10 kHz and sampled at 10–40 kHz. Stimulation electrodes were patch pipettes filled with BBS, placed close to MHb cell dendrites to activate the excitatory inputs (Figure 2B). Excitatory inputs were stimulated either with individual pulses (7–22 DV, 200 μs, biphasic), with 5 stimuli at 100 Hz every 15 s for the calcium imaging experiments (Figure 4D), or with trains consisting of 10 stimuli at 200 Hz every 10–20 s for NMDA current examination (Figures 5B and 5D). In all *ex vivo* experiments where glutamatergic synaptic currents were evoked electrically, SR95531 (2–5 μM) was added to the bath solution together with the mGluRII blocker LY341495 (0.5–1 μM), the gamma-aminobutyric acid, type b (GABAb) antagonist CGP55845 (1 μM), and the wide-spectrum purinergic receptor blocker CGS15943 (0.5 μM).

Calcium Imaging

Calcium imaging experiments were performed with a two-photon random-access microscope using acousto-optic deflector (AOD)-based scanning, as described previously (Otsu et al., 2014). Whole-cell patch pipettes were filled with an intracellular solution containing 135 mM $CsMeSO_3$, 4.6 mM $MgCl_2$, 10 mM HEPES, 10 mM K_2-creatine phosphate, 4 mM Na_2-ATP, 0.4 mM Na_2-GTP, and 2 mM QX-314, pH 7.35 with CsOH (~300 mOsm) and supplemented with a morphological (10 μM Alexa 594, Invitrogen) and a calcium-sensitive dye (500 μM Fluo-5F, Invitrogen). Cells were voltage-clamped at −60 mV in the whole-cell configuration at 32°C–34°C in the continuous presence of 50 μM D-(2R)-amino-5-phosphonovaleric acid (D-APV), 5 μM SR95531, 1 μM CGP55845, 0.5 μM CGS15943, and 0.25 μM LY341495. Calcium signals were acquired for 100–200 ms before repeated extracellular stimulation (5 pulses, 100 Hz) of the incoming PS input and for 1.8–2 s following stimulation onset. Dwell times of 20–30 μs per point were used. Stimulation-induced calcium transients were acquired every 15 s for 10 or 15 min before applying NASPM (20–50 μM). For data analysis, relative fluorescence was expressed as ΔG/R; i.e., variations in Fluo-5F signal change (ΔG) divided by calcium-independent Alexa 594 red fluorescence (R) (Otsu et al., 2014).

Ex Vivo and *In Vivo* Optogenetics

Stereotactic Injections

All optogenetic experiments were performed on adult (≥ 3 months old) VGluT2-Cre mice (Borgius et al., 2010). Following previously described protocols (Supplemental Experimental Procedures), mice were injected with either an AAV2/1.EF1α.DIO.hChR2.eYFP or an AAV2/1.EF1α.DIO.eYFP virus in the PS at the following coordinates from bregma: mediolateral (ML), 0.0 mm; anteroposterior (AP), −0.13–0.2 mm; dorsoventral (DV), −2.6 mm. Cannula implantations for *in vivo* optogenetics experiments were performed as described previously (Giber et al., 2015).

Ex Vivo Optogenetics Stimulations

Brief (1- to 2-ms-long) flashes of blue light were provided by a 470-nm wavelength light-emitting diode (LED) (Thorlabs, France) coupled to the slice chamber via the epifluorescence pathway of the microscope.

In Vivo Optogenetic Experiments: Open Field Test

The custom optical system used for fiberoptic light delivery in freely moving mice has been described in the detail previously (Giber et al., 2015). Cannula-implanted, fiberoptic-connected mice were filmed while moving freely in a round open-field arena. After 5 min of free movement in the arena, optogenetic stimulation was activated for 3 min using either a continuous train at 20 Hz or periodic laser-on (20 Hz, 1 s)/laser-off (2 s) periods (Results). After the end of stimulation, the mice were left in the arena for another 5 min. The intermittent protocol was also examined following intraperitoneal injection of LY341495 (1–4 mg/kg) dissolved in saline (9% NaCl in water). Videos were analyzed offline with Ethovision (Noldus, the Netherlands). Raw data were further analyzed in Igor Pro (Wavemetrics, USA). Total distances traveled in the minute before laser onset and between 30 s and 90 s following stimulation onset were quantified and statistically compared between the different conditions.

In Vivo Optogenetic Experiments: EPM

The EPM test was performed using a standard apparatus with transparent plastic walls delimiting the enclosed sections (Imetronics, France; Supplemental Experimental Procedures). After connecting the fiberoptic to the implanted cannula, mice freely explored the EPM for 13 min. Light stimulation was activated between minutes 5 and 8. Videos were analyzed offline with Ethovision.

In Vivo Optogenetic Experiments: MB

For this test, 24 steel marbles (1 cm in diameter) were placed on fresh bedding in a transparent plastic box. Mice were left in their home cage 15 min after linking the patchcord to the implanted cannula. They were then introduced into the box and allowed to roam freely during intermittent laser stimulation trains. The number of marbles completely buried after 10 min was quantified.

In Vivo Recordings of PS Firing Patterns

The procedures for *in vivo* recordings of septal spike patterns are described in detail in the Supplemental Experimental Procedures. Briefly, isoflurane-anesthetized mice were placed in a stereotaxic apparatus. The activity of MHb-projecting single units was recorded extracellularly in the PS (Figure 1; AP, 0.0–0.2 mm; ML, 0.0–0.1 mm; DV, 2.6–3.1), with glass micropipettes filled with 2% pontamine sky blue dissolved in 0.5 M sodium acetate (impedance, 3–6 MΩ). MHb-projecting PS units were identified using high-frequency collision methods (Glangetas et al., 2013) following antidromic activation via a stimulating electrode placed in the MHb (AP, −1.5 mm; ML, 0.3 mm; DV, 2.8 mm; with a rostro-caudal inclination of 10°). Filtered signals (band-pass, 500–5,000 Hz) were pre-amplified, amplified, and displayed on a digital storage oscilloscope. Experiments were sampled on- and offline by a computer connected to a Cambridge Electronic Design (CED) Power 1401 laboratory interface running the Spike2 software. Single units were isolated, and the spontaneous activity was recorded for 5 min. At the end of each experiment, the electrode placement was marked with an iontophoretic ejection of pontamine sky blue dye and identified *post hoc* on serial sections of the paraformaldehyde (PAF)-fixed brains. See the Supplemental Experimental Procedures for a list of the analyzed parameters and for identification criteria of bursting activity.

Immunohistochemistry

Detailed descriptions of the procedures for tissue preparation and labeling and of the antibodies used can be found in the Supplemental Experimental Procedures. The procedures followed previously described protocols (Giber et al., 2015).

Drug Application

DCG-IV (10 μM), 3,5-Dihydroxyphenylglycine (DHPG) (50 μM), and L-AP4 (200 μM) were puffed onto cells. LY341495 was both bath-applied (0.25–1 μM) and injected intraperitoneally (1–4 mg/kg) into mice for *in vivo* experiments. All other drugs were bath-applied: NBQX (10 μM), D-AP5 (50 μM), CGP55845 (1 μM), CGS15943 (0.5 μM), TBOA (100 μM), NASPM (50 μM), SR95531 (2–5 μM), minocycline (50 nM), Zn^{2+} (a free concentration of 300 nM was obtained by adding 60 μM Zn^{2+} and 10 mM tricine; Vergnano et al., 2014), Ro25-6981 (1 μM), and ClQ (20 μM). NBQX, APV, SR95531, and minocycline were from Abcam (UK). DCG-IV, DHPG, CGP55845, CGS15943, TBOA, NASPM, L-AP4, and LY341495 were from Tocris Bioscience (UK). All other drugs were from Sigma-Aldrich (France). Ro25-6981 was a kind gift from P. Paoletti (IBENS, Paris).

Data Analysis

Data analysis was performed with pClamp 10 (Molecular Devices), Origin 6.1 software (OriginLab, Northampton, USA), with custom routines written in Igor

(Wavemetrics, USA), and Ethovision (Noldus, the Netherlands). Two-photon images analyses were performed in Igor.

Statistical Analysis

The results are presented as mean ± SEM throughout the manuscript and in all figures. For statistical analyses, Mann-Whitney *U* test and Wilcoxon signed-rank test were used as appropriate. Statistical significance was set at 0.05.

SUPPLEMENTAL INFORMATION

Supplemental Information includes Supplemental Experimental Procedures and four figures and can be found with this article online at https://doi.org/10.1016/j.celrep.2017.12.064.

ACKNOWLEDGMENTS

The authors would like to thank P. Paoletti for providing GluN2AKO mice and Ro25-6981 and M. Galante, R. Lambert, N. Leresche, and E. Schwartz for critically reading the manuscript. M.A.D. was supported by funding from CNRS, INSERM, and the French Agence Nationale de la Recherche (International ANR White Program: CSD8 2009 and ANR-17-CE16-0014-01). M.M. was funded by European Research Council Starting Grant SalienSy 335333.

AUTHOR CONTRIBUTIONS

M.A.D. conceived, developed, and supervised the project. M.A.D. and Y.O. performed and analyzed the *ex vivo* electrophysiological experiments. M.A.D performed and analyzed the behavioral tests. M.A.D., Y.O., and P.M. performed the calcium imaging experiments. C.V.R. and K.P. performed immunohistochemistry. M.A.D, K.P., and C.M.-H. performed viral injections, and M.A.D. and G.P.D. implanted mice for *in vivo* optogenetic tests. S.L. performed the *in vivo* recordings in the PS under the supervision of M.M. M.A.D. wrote the manuscript, which was edited by all authors.

DECLARATION OF INTERESTS

The authors declare no competing interests.

Received: March 13, 2017
Revised: September 26, 2017
Accepted: December 20, 2017
Published: January 16, 2018

REFERENCES

Aizawa, H., Kobayashi, M., Tanaka, S., Fukai, T., and Okamoto, H. (2012). Molecular characterization of the subnuclei in rat habenula. J. Comp. Neurol. *520*, 4051–4066.

Amaral, D.G., Scharfman, H.E., and Lavenex, P. (2007). The dentate gyrus: fundamental neuroanatomical organization (dentate gyrus for dummies). Prog. Brain Res. *163*, 3–22.

Borgius, L., Restrepo, C.E., Leao, R.N., Saleh, N., and Kiehn, O. (2010). A transgenic mouse line for molecular genetic analysis of excitatory glutamatergic neurons. Mol. Cell. Neurosci. *45*, 245–257.

Choi, K., Lee, Y., Lee, C., Hong, S., Lee, S., Kang, S.J., and Shin, K.S. (2016). Optogenetic activation of septal GABAergic afferents entrains neuronal firing in the medial habenula. Sci. Rep. *6*, 34800.

Chou, M.Y., Amo, R., Kinoshita, M., Cherng, B.W., Shimazaki, H., Agetsuma, M., Shiraki, T., Aoki, T., Takahoko, M., Yamazaki, M., et al. (2016). Social conflict resolution regulated by two dorsal habenular subregions in zebrafish. Science *352*, 87–90.

Edwards, F.A., Gibb, A.J., and Colquhoun, D. (1992). ATP receptor-mediated synaptic currents in the central nervous system. Nature *359*, 144–147.

Fowler, C.D., Lu, Q., Johnson, P.M., Marks, M.J., and Kenny, P.J. (2011). Habenular α5 nicotinic receptor subunit signalling controls nicotine intake. Nature *471*, 597–601.

Frahm, S., Slimak, M.A., Ferrarese, L., Santos-Torres, J., Antolin-Fontes, B., Auer, S., Filkin, S., Pons, S., Fontaine, J.F., Tsetlin, V., et al. (2011). Aversion to nicotine is regulated by the balanced activity of β4 and α5 nicotinic receptor subunits in the medial habenula. Neuron *70*, 522–535.

Gardon, O., Faget, L., Chu Sin Chung, P., Matifas, A., Massotte, D., and Kieffer, B.L. (2014). Expression of mu opioid receptor in dorsal diencephalic conduction system: new insights for the medial habenula. Neuroscience *277*, 595–609.

Giber, K., Diana, M.A., Plattner, V., Dugué, G.P., Bokor, H., Rousseau, C.V., Maglóczky, Z., Havas, L., Hangya, B., Wildner, H., et al. (2015). A subcortical inhibitory signal for behavioral arrest in the thalamus. Nat. Neurosci. *18*, 562–568.

Glangetas, C., Girard, D., Groc, L., Marsicano, G., Chaouloff, F., and Georges, F. (2013). Stress switches cannabinoid type-1 (CB1) receptor-dependent plasticity from LTD to LTP in the bed nucleus of the stria terminalis. J. Neurosci. *33*, 19657–19663.

Görlich, A., Antolin-Fontes, B., Ables, J.L., Frahm, S., Slimak, M.A., Dougherty, J.D., and Ibañez-Tallon, I. (2013). Reexposure to nicotine during withdrawal increases the pacemaking activity of cholinergic habenular neurons. Proc. Natl. Acad. Sci. USA *110*, 17077–17082.

Hamann, M., and Attwell, D. (1996). Non-synaptic release of ATP by electrical stimulation in slices of rat hippocampus, cerebellum and habenula. Eur. J. Neurosci. *8*, 1510–1515.

Hatton, C.J., and Paoletti, P. (2005). Modulation of triheteromeric NMDA receptors by N-terminal domain ligands. Neuron *46*, 261–274.

Herkenham, M., and Nauta, W.J. (1977). Afferent connections of the habenular nuclei in the rat. A horseradish peroxidase study, with a note on the fiber-of-passage problem. J. Comp. Neurol. *173*, 123–146.

Herkenham, M., and Nauta, W.J. (1979). Efferent connections of the habenular nuclei in the rat. J. Comp. Neurol. *187*, 19–47.

Hikosaka, O. (2010). The habenula: from stress evasion to value-based decision-making. Nat. Rev. Neurosci. *11*, 503–513.

Hsu, Y.W., Tempest, L., Quina, L.A., Wei, A.D., Zeng, H., and Turner, E.E. (2013). Medial habenula output circuit mediated by α5 nicotinic receptor-expressing GABAergic neurons in the interpeduncular nucleus. J. Neurosci. *33*, 18022–18035.

Kim, U., and Chang, S.Y. (2005). Dendritic morphology, local circuitry, and intrinsic electrophysiology of neurons in the rat medial and lateral habenular nuclei of the epithalamus. J. Comp. Neurol. *483*, 236–250.

Kim, U., and Chung, L.Y. (2007). Dual GABAergic synaptic response of fast excitation and slow inhibition in the medial habenula of rat epithalamus. J. Neurophysiol. *98*, 1323–1332.

Koppensteiner, P., Galvin, C., and Ninan, I. (2016). Development- and experience-dependent plasticity in the dorsomedial habenula. Mol. Cell Neurosci. *77*, 105–112.

Otsu, Y., Marcaggi, P., Feltz, A., Isope, P., Kollo, M., Nusser, Z., Mathieu, B., Kano, M., Tsujita, M., Sakimura, K., and Dieudonné, S. (2014). Activity-dependent gating of calcium spikes by A-type K+ channels controls climbing fiber signaling in Purkinje cell dendrites. Neuron *84*, 137–151.

Paoletti, P., Bellone, C., and Zhou, Q. (2013). NMDA receptor subunit diversity: impact on receptor properties, synaptic plasticity and disease. Nat. Rev. Neurosci. *14*, 383–400.

Qin, C., and Luo, M. (2009). Neurochemical phenotypes of the afferent and efferent projections of the mouse medial habenula. Neuroscience *161*, 827–837.

Ren, J., Qin, C., Hu, F., Tan, J., Qiu, L., Zhao, S., Feng, G., and Luo, M. (2011). Habenula "cholinergic" neurons co-release glutamate and acetylcholine and activate postsynaptic neurons via distinct transmission modes. Neuron *69*, 445–452.

Robertson, S.J., and Edwards, F.A. (1998). ATP and glutamate are released from separate neurones in the rat medial habenula nucleus: frequency dependence and adenosine-mediated inhibition of release. J. Physiol. *508*, 691–701.

Robertson, S.J., Burnashev, N., and Edwards, F.A. (1999). Ca2+ permeability and kinetics of glutamate receptors in rat medial habenula neurones: implications for purinergic transmission in this nucleus. J. Physiol. *518*, 539–549.

Soria-Gómez, E., Busquets-Garcia, A., Hu, F., Mehidi, A., Cannich, A., Roux, L., Louit, I., Alonso, L., Wiesner, T., Georges, F., et al. (2015). Habenular CB1 Receptors Control the Expression of Aversive Memories. Neuron *88*, 306–313.

Stephenson-Jones, M., Floros, O., Robertson, B., and Grillner, S. (2012). Evolutionary conservation of the habenular nuclei and their circuitry controlling the dopamine and 5-hydroxytryptophan (5-HT) systems. Proc. Natl. Acad. Sci. USA *109*, E164–E173.

Vergnano, A.M., Rebola, N., Savtchenko, L.P., Pinheiro, P.S., Casado, M., Kieffer, B.L., Rusakov, D.A., Mulle, C., and Paoletti, P. (2014). Zinc dynamics and action at excitatory synapses. Neuron *82*, 1101–1114.

Wang, H., Peca, J., Matsuzaki, M., Matsuzaki, K., Noguchi, J., Qiu, L., Wang, D., Zhang, F., Boyden, E., Deisseroth, K., et al. (2007). High-speed mapping of synaptic connectivity using photostimulation in Channelrhodopsin-2 transgenic mice. Proc. Natl. Acad. Sci. USA *104*, 8143–8148.

Yamaguchi, T., Danjo, T., Pastan, I., Hikida, T., and Nakanishi, S. (2013). Distinct roles of segregated transmission of the septo-habenular pathway in anxiety and fear. Neuron *78*, 537–544.

Zhang, J., Tan, L., Ren, Y., Liang, J., Lin, R., Feng, Q., Zhou, J., Hu, F., Ren, J., Wei, C., et al. (2016). Presynaptic Excitation via GABAB Receptors in Habenula Cholinergic Neurons Regulates Fear Memory Expression. Cell *166*, 716–728.

Cell Reports, Volume *22*

Supplemental Information

Functional Principles of Posterior Septal Inputs to the Medial Habenula

Yo Otsu, Salvatore Lecca, Katarzyna Pietrajtis, Charly Vincent Rousseau, Païkan Marcaggi, Guillaume Pierre Dugué, Caroline Mailhes-Hamon, Manuel Mameli, and Marco Alberto Diana

SUPPLEMENTAL INFORMATION

SUPPLEMENTAL EXPERIMENTAL PROCEDURES

All procedures involving experimental animals were performed in accordance with the Directive 2010/63/EU, and local ethics committee guidelines. All efforts were made to minimize animal suffering and the number of animals used.

Slice preparation

All mice used were more than 3 months old. Coronal brain slices (300 µm) including the MHb and the dorsal hippocampus (Fig.2) were prepared from either C57/B6 mice, GluN2KO mice or their control littermates (C57/B6 genetic background), VGluT2-Cre mice (C57/B6 background), or, finally, from Thy1-ChR2 mice (line 18; Wang et al., 2007). Following deep anesthesia with isoflurane, the brain was quickly removed in an ice-cold bicarbonate-buffered (BBS) solution containing the following (mM): 116 NaCl, 2.5 KCl, 1.25 NaH_2PO_4, 25.7 $NaHCO_3$, 30 glucose, 2 $CaCl_2$, 1.5 $MgCl_2$, and 5×10^{-5} minocycline (bubbled with 95% O_2, 5% CO_2). Slices were cut using a vibrating blade microtome (Campden model 7000smz2) in an ice-cold solution containing the following (mM): 130 K-gluconate, 15 KCl, 2 EGTA, 20 HEPES, 25 glucose, 1 $CaCl_2$, 6 $MgCl_2$ and 0.05 D-(−)-2-amino-5-phosphonovaleric acid (D-APV) (pH 7.4 with NaOH), and were then transiently immersed in a modified BBS, as follows (mM): 225 D-mannitol, 2.5 KCl, 1.25 NaH_2PO_4, 25 $NaHCO_3$, 25 glucose, 1 $CaCl_2$, 6 $MgCl_2$ and 0.05 D-APV (25°C, bubbled with 95% O_2, 5% CO_2). Finally slices were transferred to warm BBS (32°-34°C) for the rest of the experimental day.

Electrophysiology

For electrophysiological recordings, slices were moved to a recording chamber mounted on an upright Slicescope (Scientifica, Uckfield, UK) and continuously perfused with bubbled BBS (~2 ml/min; 30–34°C).
We recorded neurons located exclusively in the ventral part of the MHb (vMHb). Cells were visualized with a combination of Dodt contrast, and an on-line video contrast enhancement. Tight-seal cell-attached (CA), whole-cell (WC), and loose cell-attached (LCA) recordings were performed with an EPC-10 double amplifier (Heka Elektronik, Lambrecht/Pfalz, Germany) run by PatchMaster software (Heka). MHb cells could be easily identified in the transmitted deep red light (~750 nm) with which slices were visualized using a CoolSnap HQ^2 CCD camera (Photometrics, Trenton, NJ) run by MetaMorph (Universal Imaging, Downington, PA). For WC recordings, patch pipettes (resistance 2.5-4MΩ) were filled with an intracellular solution containing (mM): 150 $CsMeSO_3$ (Sigma), 10 TEA·Cl, 1 $CaCl_2$, 4.6 $MgCl_2$, 10 HEPES, 10 K_2-creatine phosphate (Calbiochem), 0.5 EGTA , 4 Na_2-ATP, 0.4 Na_2-GTP, 0.1 spermine and 2 QX-314, pH 7.35 with CsOH (~300 mOsm), sometimes supplemented with a morphological dye (5µM Alexa 488, Invitrogen) to check cell morphology. For current clamp recordings (Fig.S2), and experiments examining DCG-IV-induced currents in WC, the intracellular solution contained as follows (mM): 150 K-Gluconate, 4 NaCl, 10 Hepes, 10 K_2-phosphocreatine, 0.1 K_3EGTA, 6 Mg_2ATP, 0.4 NaGTP. In the WC configuration, series resistance was partially compensated (max 65%), whereas liquid junction potentials were not corrected. Loose Cell Attached (LCA; seal resistance: 15-20 MΩ) recordings were performed at a holding potential at -60 mV, with pipettes of resistance comprised between 2.5 and 5 MΩ) filled with an HEPES-buffered solution (HBS) containing (mM): 130 NaCl, 2.5 KCl, 1.25 NaH_2PO_4, 30 glucose, 2 $CaCl_2$, 1.5 $MgCl_2$, 10 HEPES, pH 7.35 with NaOH (~300 mOsm). Currents were filtered at 10 kHz and sampled at 10-40 kHz. Stimulation electrodes were patch pipettes filled with ACSF and put in the vicinity of MHb cell dendrites to activate the excitatory inputs. The MHb lacks a spatially precise, reciprocal organization of incoming axonal fibers and postsynaptic dendrites. As a consequence, after establishing the WC configuration the search for synaptic responses had variable duration, ranging from a few seconds to several minutes. When found, transmission originated from single presynaptic axons (see Fig.2). Excitatory inputs were stimulated either with individual pulses (7-22 V, 200 µs, biphasic), or with 5 stimuli at 100Hz every 15s for the calcium imaging experiments (Fig.4), or with trains consisting of 10 stimuli at 200 Hz every 10-20 sec for NMDA current examination (Fig.5B&D). This latter protocol closely reproduced the average intra-burst firing frequency of PS neurons (Fig.1). Furthermore, this stimulation pattern was necessary in order to maximize synaptic summation, reduce inter-trial variability, and thus minimize the number of trial repetitions at potentials where recordings of MHb cells rapidly deteriorated (between -20mV and +10mV). In all *ex vivo* experiments where glutamatergic synaptic currents were evoked electrically, SR95531 (2-5µM) was added to the bath solution, together with the mGluRII blocker LY341495 (0.5/1µM), the GABAb antagonist CGP55845 (1µM), and the wide spectrum purinergic receptor blocker CGS15943 (0.5µM).

Calcium imaging

Whole-cell patch pipettes were filled with an intracellular solution containing (in mM): 135 $CsMeSO_3$ (Sigma), 4.6 $MgCl_2$, 10 HEPES, 10 K_2-creatine phosphate (Calbiochem), 4 Na_2-ATP, 0.4 Na_2-GTP, 2 QX-314, pH 7.35 with CsOH (~300 mOsm) and supplemented with a morphological (10µM Alexa 594, Invitrogen) and a calcium-

sensitive dye (500 µM Fluo-5F, Invitrogen). Cells were voltage-clamped at -60 mV in the WC configuration via a Multiclamp700B amplifier (Molecular devices, Sunnyvale, USA). The series resistance was partially compensated (~60%). WC currents were filtered at 1-2 kHz, and sampled at 10 kHz. Imaging was done at 32-34°C (Single Channel Heater Controller, Warner Instruments) in the continuous presence of (µM): 50 D-APV, 5 SR95531, 1 CGP55845 and 0.5 CGS15943, 0.25 LY341495. Calcium signals in MHb cell dendrites were monitored by two-photon random-access microscopy using acousto-optic deflector (AOD)-based scanning (Otsu et al., 2014). In this instrument, both X and Y scannings are operated by acousto-optic deflectors (AODs). These non-mechanical beam-steering devices (A-A Opto-Electronic) can redirect the laser beam in 10µs. To operate the AODs and run the scanning procedures, a custom-made user interface was programmed in LabView (National Instruments). The AOD acoustic frequency drive was generated by a Direct Digital Synthesizer and a fast (10ns) power amplifier (A-A Optoelectronics). Two-photon excitation was produced by an infrared Ti-Sa pulsed laser tuned to 825nm by a Chamaelon-XR (Coherent) coupled to a microscope (Slicescope, Scientifica). The microscope was equipped with a 25×/0.95NA objective (LUMPlanFL/IR, Leica microsystems). Fluorescence photons were detected by cooled AsGaP H10769PA–40 photomultipliers (Hamamatsu) in the transfluorescence and epifluorescence pathways, with a 641/75 nm bandpass filter (Semrock) to see the cell morphology, and a 510/84 nm bandpass filter (Semrock) to acquire calcium signals (Otsu et al., 2014).
Firstly, a synaptic input was searched for by moving the stimulation pipette in the area surrounding the recorded cell, using short stimulation trains (5 pulses at 100Hz). Once found the input, regions of interest (ROIs) were chosen in such a way to cover as large a dendritic area as possible in the available field of view. If no calcium increase was detected, the focus plane was changed and new ROIs on other sections of the dendritic processes were set until a calcium signal was clearly recorded. Calcium signals were acquired for 100-200ms before electrical stimulation of the incoming septal input and, for 1.8-2s following stimulation onset. Dwell times of 20-30µs per point were used. Calcium signals were sampled every 0.9-1.2ms.
To perform stable, long-duration multipoint acquisitions, registration of the field of view was implemented online between each episode of stimulation by 3D correlation between the image of a small field and a previously acquired 3D stack of the same region. Stimulation-induced calcium transients were acquired every 15s for 10/15 min before applying NASPM (20-50µM). The effect of NASPM was monitored in the following 10-15minutes.
For data analysis, relative fluorescence was expressed as ΔG/R, i.e. variations in Fluo-5F signals change (ΔG) divided by calcium-independent Alexa 594 red fluorescence (R). This ratiometric method scales the calcium fluorescence signal to the volume of the imaged compartment, yielding a measurement of the dye-bound cytoplasmic calcium concentration independent of dendritic geometry (Otsu et al., 2014). Image analysis was performed in Igor (Wavemetrics, Lake Oswego, USA).

Ex vivo and _in vivo_ optogenetics

Stereotactic injections

All optogenetic experiments were performed on adult (≥ 3 month-old) VGluT2-Cre mice (Borgius et al., 2010) obtained via the European Mouse Mutant (EMMA) Archive. Mice were anesthetized with an intraperitoneal injection of ketamine-xylazine (200 and 10 mg/kg, respectively) and placed inside a stereotactic apparatus (Kopf Instruments, Tujunga, CA). An AAV2/1-EF1α-DIO.hChR2(H134R).eYFP virus, based on Addgene plasmid 20298 and produced at the Laboratory of Gene Therapy (INSERM UMR 1089, Nantes, France), was injected in the posterior septum, at the following coordinates: Bregma ML: 0.0mm ; AP, -0.13-0.2mm; DV, -2.6mm. For the *in vivo* control experiments described in Fig.7, posterior septal neurons were transfected using an AAV2/1-EF1α-DIO.eYFP virus, based on Addgene plasmid 27056, and produced by the Vector Core facility of the University of Pennsylvania.
Injections were performed using pipettes pulled from graduated capillaries, at a rate of 100-150 nl/min for a total volume of around 300/500nL. All optogenetic experiments were all performed at least four weeks after viral injection.
Concerning cannula implantations for *in vivo* experiments, four weeks after transfection of posterior septal cells with either a hChR2-eYFP or an eYFP expressing virus, VGluT2-Cre animals were re-anaesthetized with ketamine-xylazine (100 and 5 mg/kg) and placed in a stereotactic frame. Once exposed, the skull was cleaned with H_2O_2 and covered with a layer of Super Bond C&B (Morita, Dietzenbach, Germany). A craniotomy was performed and an optic fiber (200 µm, 0.53 NA, 3mm) housed inside a connectorized implant (M3, Doric Lenses, Quebec, Canada) was lowered over the MHb (Bregma -1.5 AP, +0.0 ML,-2.2/-2.5 DV). The craniotomy was covered with a drop of warm agarose gel (2%), and the implant was secured with dental acrylic (Pi-Ku-Plast HP 36, Bredent, Senden, Germany). The skin was stitched at the rear and front of the implant and the animal was allowed to recover on a heating pad. Mice were allowed to recover for at least 5 days before testing.

Ex vivo optogenetics stimulations

The brief (1-2 ms long) flashes of blue light used to evoke leEPSCs were provided by triggering a 470 nm-wavelength LED (Thorlabs, Maisons-Laffitte, France) coupled to the slice chamber via the epifluorescence

pathway of the microscope. The effect of optogenetic stimulation in slices was studied by recording cells in either the WC, or the LCA configuration as described.

In vivo optogenetic experiments

The custom optical system used for fiber optic light delivery in freely moving mice was described previously (Giber et al., 2015). Briefly, the beam generated by a 473 nm DPSS laser (LRS-0473-PFM-00100-03, Laserglow Technologies, Toronto, Canada) was passed through an acousto-optic tunable filter (AOTFnC-400.650-TN, AA Opto-Electronic, Orsay, France) controlled by a multi digital synthesizer (MDS4C-D66-22-74.158-RS). The first order beam exiting the AOTF was bounced on mirrors and directed into the core of a fiber optic patchcord (200 μm, 0.37NA) through a custom table-top rotary joint (Doric). The patchcord (1.6 m) was connected to the mouse cannula and allowed to rotate passively. With adequate beam alignment, rotations induced power fluctuations of less than 5% at the fiber output.
During each session, mice movement was filmed continuously via a CCD camera (Scout scA640-74, Basler, Ahrensburg, Germany). All aspects of the experiment (photostimulation waveform generation, MDS and LED control, video recordings) were controlled using LabVIEW (National Instruments Corporation, Austin, TX).

Open field test.
Cannula-implanted mice were housed in individual cages. Before being introduced into the arena, the animals were allowed to get acquainted to the experimental room and its light conditions (~30lux) for at least 60min. Mice were then connected to the patchcord, and allowed to move freely in a gray, round open field arena (38cm diameter, 15cm wall height, Noldus, Wageningen, Holland) while being filmed. After 5min of free movement in the arena, optogenetic stimulation was activated for 3min using either a continuous 20Hz train, or alternate laser-on (20Hz, 1s) / laser-off (2s) periods (see results). After end of stimulation, the mice were left in the arena for 5 more minutes. The periodic protocol was also examined on mice following (minimum 90min) intraperitoneal injection of LY341495 (1-4mg/Kg) dissolved in saline (9% NaCl in distilled water; Scofield et al., 2015). Injection of LY341495 did not *per se* affected locomotion. Indeed, the total distances travelled by AAV2/1-DIO.hChR2-eYFP injected VGluT2-Cre mice in the minute preceding laser onset were 326.5±33.4cm and 255.9±40.4cm for the intermittent protocol in naïve (i.d.: not i.p. injected) and LY341495 injected mice ($p=0.11$), respectively.
Individual experimental sessions were performed at least at one week distance. Movies were analyzed off-line with Ethovision (Noldus). Raw data were then exported, and further analyzed in Igor Pro 5.0 (Wavemetrics, Lake Oswego, USA). Total distances traveled in the minute before laser stimulation onset, and between 30s and 90s following light onset were quantified, and statistically compared between the different conditions indicated in the text.

Elevated plus maze.
The Elevated Plus Maze (EPM) test was performed using a standard apparatus (arm length: 65cm x 65cm, height: 47.5cm; Imetronic, Pessac, France) with transparent plastic walls delimiting the enclosed sections. Mice got accustomed to the experimental room light level in their home cage for at least 1 hour prior to testing. The laser-connected patchcord was then screwed to the implanted cannula, and the mouse was allowed to freely explore the EPM for 13 minutes. Alternated light stimulation (1s/on, 2s/off) was activated between minutes 5 and 8 during the test. Videos were analyzed off-line with Ethovision (Noldus).

Marble burying.
For this test, 3 rows of 8 steel marbles (diameter: 1cm) were placed on fresh bedding in a transparent plastic box (44cm long, 28cm large). Mice got accustomed to the experimental room light level in their home cage for at least 1 hour prior to testing, and 15 more minutes following fixation of the patchcord to the implanted cannula. They were then introduced in the box and allowed to roam freely during periodic light trains (1s/on, 2s/off). The number of marbles completely buried after 10 minutes was quantified.

In vivo recordings of posterior septal firing patterns
Mice were anesthetized with isoflurane (Univentor, Malta. Induction: 2%; maintenance: 1-1.5%), and placed in a stereotaxic apparatus (Kopf, Germany). Their body temperature was maintained at 36±1°C using a heating pad (CMA 450 Temperature Controller, USA). The scalp was retracted and one burr hole was drilled above the posterior septum (AP: 0.0–0.2 mm, ML: 0.0–0.1 mm, DV: 2.6–3.1) for the placement of a recording electrode. For identifying MHb-projecting septal neurons with antidromic stimulation, a bipolar concentric electrode was lowered in the MHb (AP: -1.5 mm, ML: 0.3 mm, DV: 2.8 mm), with a 10° inclination in the rostro-caudal axis.
Single unit activity was recorded extracellularly by glass micropipettes filled with 2% pontamine sky blue dissolved in 0.5 M sodium acetate (impedance 3–6 MΩ). Signals were filtered (band-pass 500–5000 Hz), pre-

amplified (DAM80, WPI, Germany), amplified (Neurolog System, Digitimer, UK), and displayed on a digital storage oscilloscope (OX 530, Metrix, USA).
Experiments were sampled on- and off-line by a computer connected to a CED Power 1401 laboratory interface (Cambridge Electronic Design, Cambridge, UK) running the Spike2 software (Cambridge Electronic Design). Single units were isolated and the spontaneous activity was recorded for 5min.
Spontaneous firing rate, percentage of spikes in bursts, mean spikes per burst, mean burst duration, mean intra-burst frequency and coefficient of variation (CV=standard deviation of interspike intervals divided by the mean interspike interval) were determined. Criteria for burst identification were chosen via qualitative analysis of the interspike interval histogram of the recorded cells. We defined as a burst a sequence of action potentials starting when 2 events occurred with an interval smaller than 20ms, and ending when the interval between 2 consecutive spikes exceeded 50ms.
MHb-projecting PS neurons were identified using high frequency collision methods (Glangetas et al., 2013), following antidromic stimulation in the MHb. Stimulation-triggered spikes were considered antidromic if they met the following criteria: 1) constant latency from stimulation onset, 2) high reliability (~100%) of antidromic stimulation at 100Hz, or greater, frequencies, and 3) collision of triggered spikes with spontaneous action potentials occurring in an interval approximately equal to the sum of the refractory period, and of the latency from stimulation.
At the end of each experiment, the electrode placement was marked with an iontophoretic deposit of pontamine sky blue dye (with a negative continuous current of 80 µA during 35 min). To mark electrical stimulation sites, positive current (10µA) was passed through the stimulation electrode for 1min. Brains were then rapidly removed and fixed in a 4% paraformaldehyde solution. The position of the electrodes was then identified on serial sections (60 µm).

Immunohistochemistry
Methods for immunohistochemical staining followed the protocols described in detail previously (Rousseau et al., 2012; Giber et al., 2015).

Tissue fixation. Adult mice were deeply anesthetized with intraperitoneal injections of sodium pentobarbital (60mg/kg), and perfused through the ascending aorta with PBS, followed by 50ml of 4% freshly depolymerized paraformaldehyde in 100mM PBS, pH 7.4, at 4°C. Brains were then dissected and postfixed in 4% paraformaldehyde overnight at 4°C, before embedding in paraffin.

Tissue preparation and labeling. Sections were cut with a thickness of 7µm. After removing paraffin, sections were processed in a decloaking chamber (Biocare Medical, Concord, CA) using a citrate-buffer-based antigen retrieval medium (Biocare Medical) for 20min at 110–115°C. They were then processed in PBS with 15% methanol and 0.3% H_2O_2 to block endogenous peroxidase activity. Aldehyde groups were removed by incubating the sections in sodium borohydride (1%) in PBS. After these treatments, the slices were incubated in a blocking PBS-based solution containing cold-water fish-skin gelatin (0.1%) and Triton X-100 (0.1%). Tissues were then incubated overnight at 4°C with the following primary antibodies: anti-VGluT2 (1:1000; Millipore), anti-GluA1 (1:500; Synaptic Systems), anti-GluA2 (1:500; Synaptic Systems), GluN1 (1:200; Millipore), GluN2A (1:100; Upstate Biotechnology), GluN2B (1:100; BD Transduction Laboratories), chicken anti-GFP (1:1000; Aves Laboratories). Primary antibodies were revealed by incubation for 2hrs with secondary antibodies coupled to either Alexa Fluor-488 (Invitrogen, Saint Aubin, France) or DyLight488, DyLight549, and DyLight649 (1:200 or 1:400; Jackson ImmunoResearch). Sections were finally mounted using Prolong Gold Antifade Reagent (Invitrogen). For all experiments, control sections were incubated without primary antibodies. Images were acquired using a confocal microscope (SP2, Leica Microsystems) with a 25×, and a 40× oil-immersion objective.

Drug application
DCGIV (10µM), DHPG (50µM), and L-AP4 (200µM) were puffed onto the cells. LY341495 was either bath applied (0.25-1µM) in slices, or injected intraperitoneally (1-4mg/Kg) in mice for *in vivo* experiments. All other drugs were bath applied: NBQX (10µM), D-AP5 (50µM), CGP55845 (1µM), CGS15943 (0.5µM), TBOA (100µM), NASPM (50µM), SR95531 (2-5µM), Zn^{2+} (a free concentration of 300nM was obtained by adding 60µM Zn^{2+} and 10mM tricine (Vergnano et al., 2014)); Ro25-6981 (1µM); CIQ (20µM). NBQX, APV, SR95531 and minocycline were from Abcam (Cambridge, UK). DCGIV, DHPG, CGP55845, CGS15943, TBOA, NASPM, L-AP4, LY341495 were from Tocris (Bristol, UK). All other drugs were from Sigma-Aldrich France (Saint-Quentin Fallavier, France). Ro25-6981 was a kind gift of P. Paoletti (IBENS, Paris).

Data analysis
Data analysis was performed with pClamp 10 (Molecular devices), Origin 6.1 software (OriginLab, Northampton, USA), with custom routines written in Igor, and Ethovision.

Statistical analysis

The results are presented as mean ± SEM throughout the manuscript, and in all figures. For statistical analyses, Mann-Whitney U test and Wilcoxon signed-rank test were used as appropriate. Statistical significance was set at 0.05.

Supplemental Figures

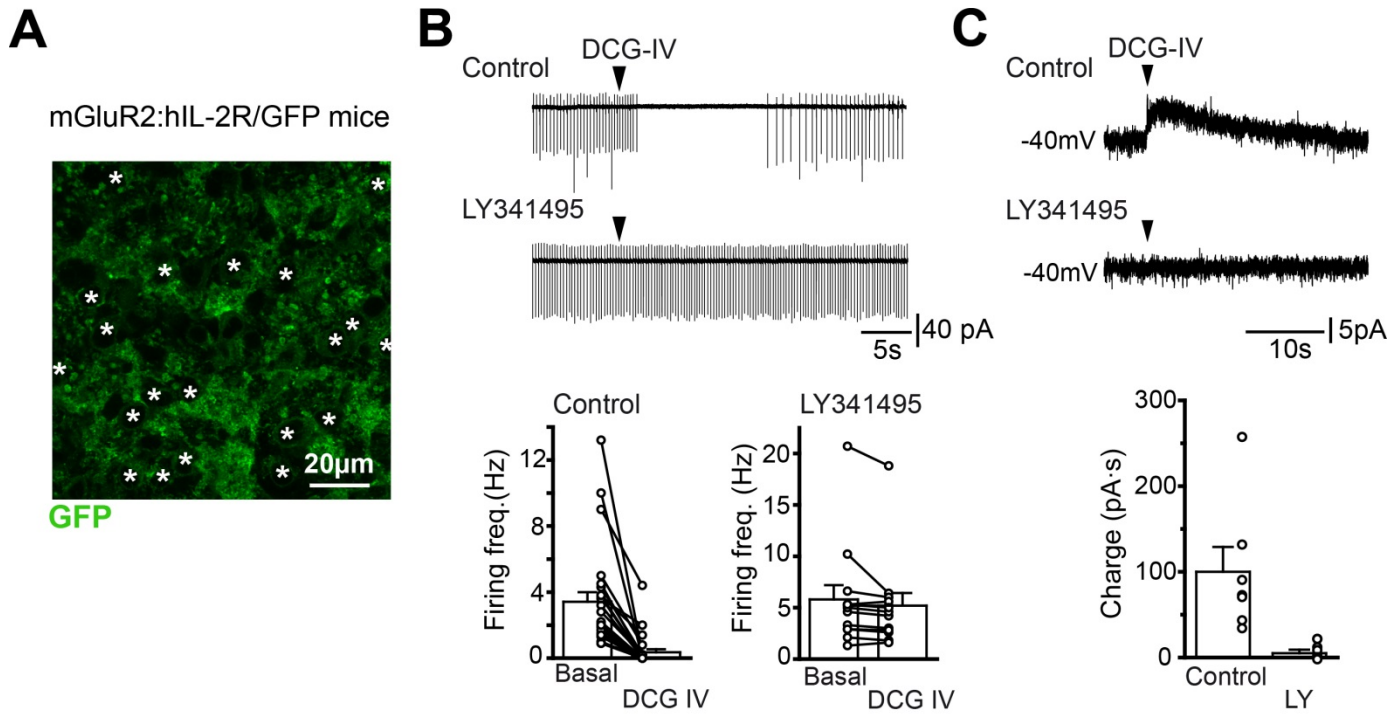

Figure S1 (related to Figure 6). Glutamate group II metabotropic receptors are expressed in MHb neurons and potently reduce spike rate.

A.Immunohistochemical staining for GFP in the MHb of a mouse expressing the human interleukin receptor 2 (hIL-R2) and GFP, under the control of the promoter of the metabotropic glutamate receptor 2 (mGluR2; Watanabe et al., 1998). mGluR2 belongs to the group II metabotropic receptor family (mGluRII). The fluorescence signal was expressed both in presynaptic structures (Yamaguchi et al., 2013), and on the cell membranes of most MHb neurons. A subset of positive cells is highlighted by white asterisks, as an example. **B.** Puffing of the mGluRII agonist DCG-IV (10µM) potently inhibited spike rate in all spontaneously firing MHb cells recorded in the LCA configuration, on average to 7.4±3.1% of the control (range: 0%-56%; n=26; $p<0.001$; see traces for a single neuron on top, and values for all the cells tested in the left bar graph below). DCG-IV action was completely absent when the mGluRII antagonist LY341495 (1µM) was applied in the bath (average firing rate: 93.4±3.7% with respect to control period; n=13; right bar graph). In contrast to mGluRII interfering agents, the group I (mGluRI) agonist DHPG (50µM) produced only a small increase of the firing frequency to 139.9±8.5% of the control, which did not reach statistical significance (n=5; p=0.06; data not shown). Furthermore, the group III (mGluRIII) agonist L-AP4 (200µM) did not induce any modification in action potential rate, which was 97.5±5.0% of the control (n=8; p=0.8; data not shown) during drug application.

C. DCG-IV puffs reliably induced outward currents in MHb cells (total transferred charge: 100.0 ± 28.9pC; n=7) when neurons were recorded in the WC configuration at -40mV. These currents were prevented by LY341495 application (9.7±4.0pC; n=6; p=0.001). See traces from a typical recording on top, and the corresponding graphs for all tested neurons below. Data are represented as mean±SEM.

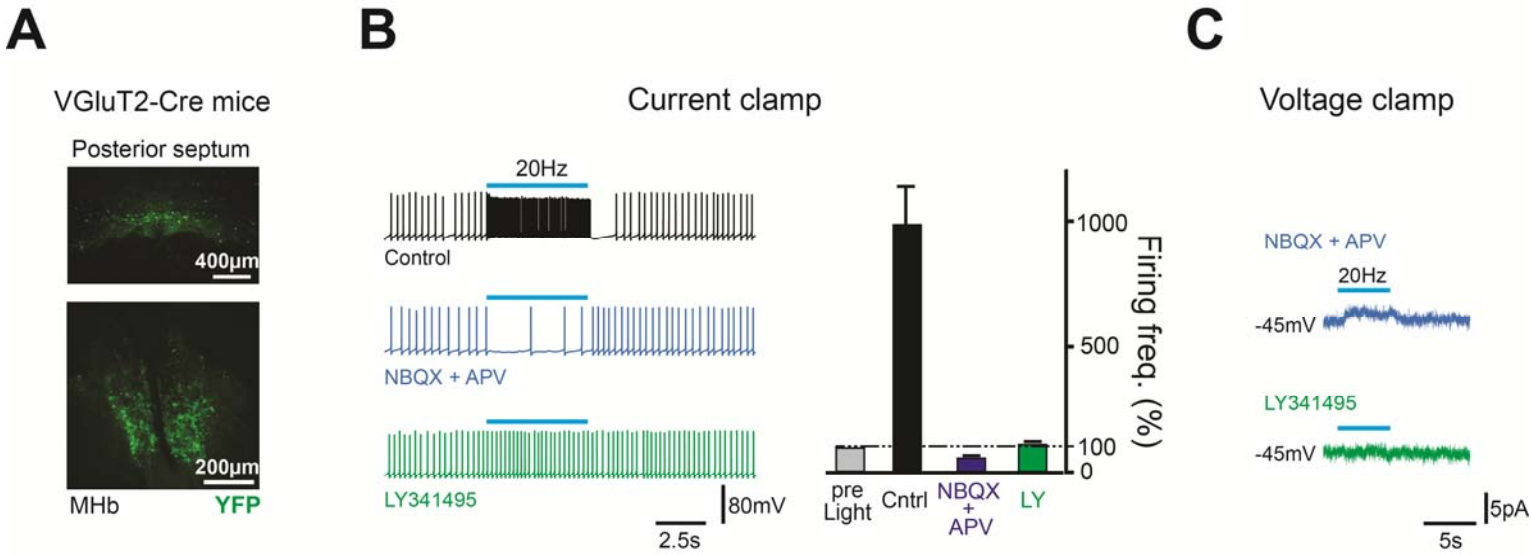

Figure S2 (related to Figure 6). Optogenetically induced modulation of firing in MHb neurons: whole cell recordings.

A. Here we show 2 typical images illustrating the site of injection in the PS (above), and the resulting fluorescence in the MHb (below) of a VGluT2-Cre mouse injected with an AAV2/1-DIO.hChR2-YFP virus. **B.** CC recordings of a MHb cell, in which a 5s-long stimulation train of light pulses at 20Hz (light blue line) triggered a dramatic increase in spike rate, followed by a prominent after-hyperpolarization (black trace, above left). On average, spike rates augmented to 989.2±146.32% of the control (n=17; p=0.0003), whereas average after-hyperpolarizations amounted to 7.0±1.0mV, and led to great inhibition of the action potential frequency, to 40.4±10.8% of the control (n=17; p=0.0007). Co-application of NBQX and APV eliminated the late inhibition completely (average spike rate: 92.3±14.2%; p=0.6; n=14). The block of ionotropic glutamate receptors also revealed a strong decrease of firing during the stimulation train, to 59.0±7.8% of the control (n=15; p=0.002; middle blue trace), which was blocked by LY341495 applications (113.5±8.4%; p=0.08; green trace). The quantification for all the tested cells is in the right bar graph. **C.** In a similar cell as in panel **B**, the stimulation train triggered a small but detectable outward current in the presence of NBQX and APV, amounting to 2.0±0.5pA (n=9; p=0.002; above blue trace), which was blocked by LY341495 (green trace below). Thus, mGluRIIs can indeed be activated by incoming synaptic activity in MHb neurons. These VC recordings were performed at a holding potential of -45mV. Data are represented as mean±SEM.

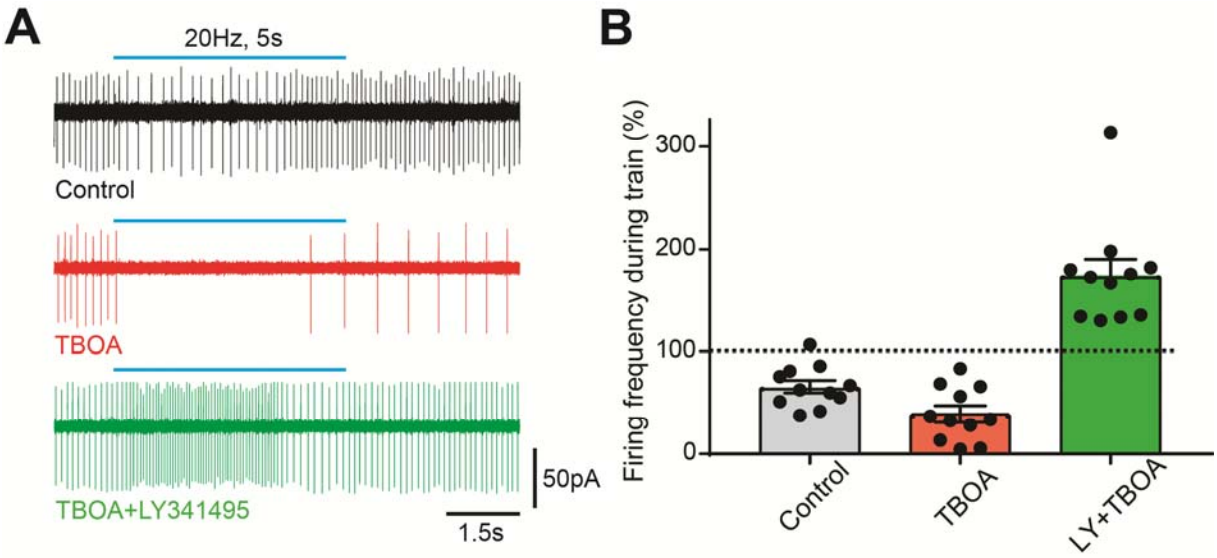

Figure S3 (Related to Figure 6). The glutamate transporter blocker TBOA potentiates the inhibitory effect of mGluRII activation on MHb cell firing.

A. In this MHb cell, a 5s-long light stimulation train at 20Hz (light blue line) reduced the spontaneous spike rate recorded in the LCA configuration (black upper trace), typical for the cell group described in Fig. 6C. Bath application of TBOA (100µM; red middle trace) potentiated the inhibitory effect. Application of the mGluRII antagonist LY341495 completely blocked the inhibition, highlighting an underlying potentiation probably due to mGluRI receptors (green lower trace). The effect of TBOA is quantified for all recorded cells in the bar graph in **B**. Data are represented as mean±SEM.

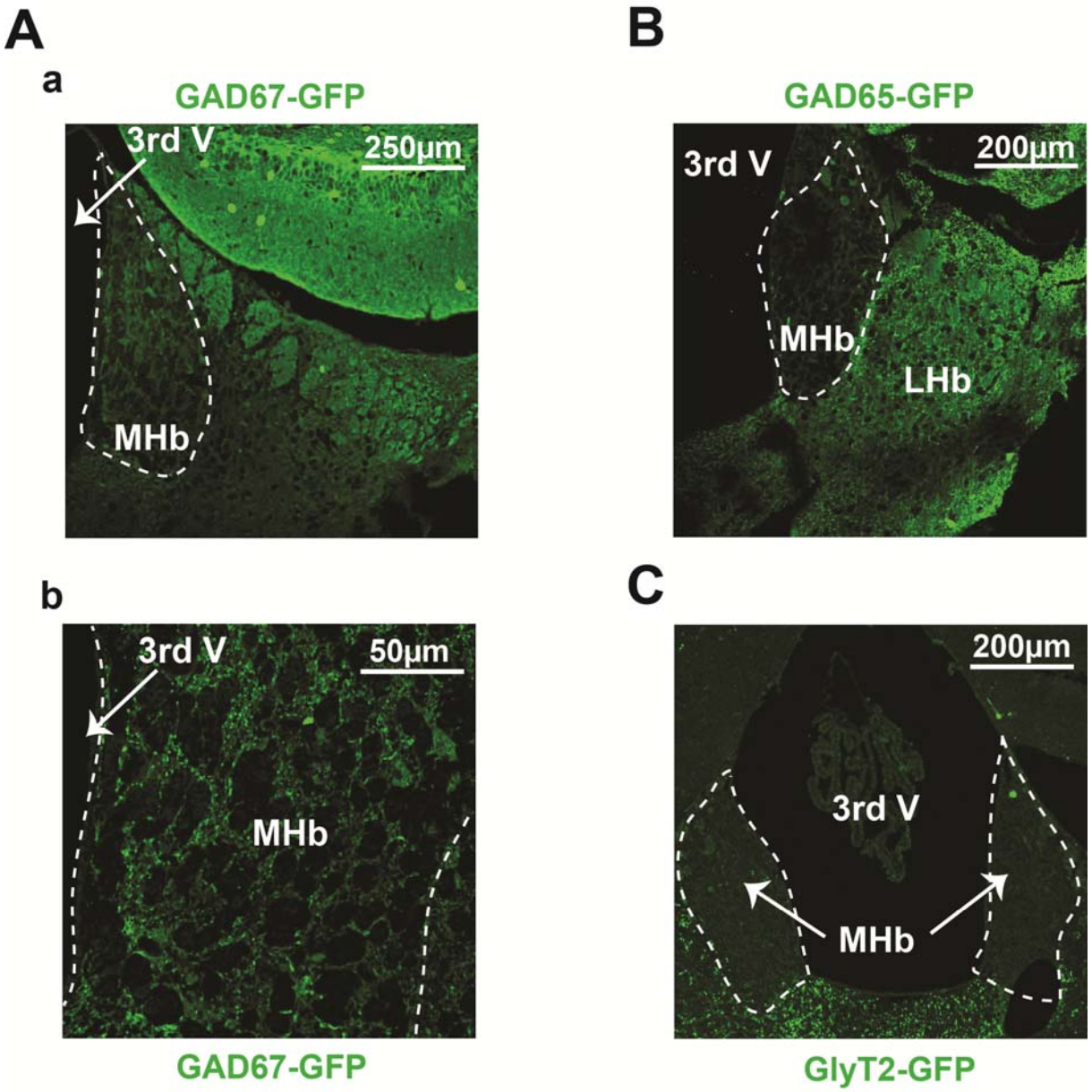

Figure S4 (related to Figure 6). The MHb is devoid of both GABAergic, and glycinergic local interneurons.

A. Typical GFP expression in the MHb and its surrounding regions of a coronal section from a GAD67-GFP mouse. In **a,** the low level of expression in the MHb can be compared with the dorsally located part of the hippocampus visible in the image. In **b,** at larger magnification, only the presence of putative axonal projections, most likely originating extrinsically from the medial septum (see Qin & Luo, 2009), can be detected. No local interneurons are present.

B. Here, a low magnification image of a coronal slice from a GAD65-GFP mouse is shown. Again, no local interneurons are present, the MHb being devoid also of the signal originating from the axonal plexuses of extrinsic origin found in GAD67-GFP mice. Note the difference in GFP level between the MHb, and the more laterally located lateral habenula (LHb).

C. Absence of both glycinergic cells and terminals in the MHb, as illustrated by a coronal section from a GlyT2-GFP animal. Note the difference of fluorescence between the MHb, and the dorsal part of the thalamic paraventricular nucleus, located just ventrally with respect to the third ventricle (3rd V; Giber et al., 2015).

Supplemental references

Borgius, L., Restrepo, C. E., Leao, R. N., Saleh, N. & Kiehn, O. 2010. A transgenic mouse line for molecular genetic analysis of excitatory glutamatergic neurons. *Mol Cell Neurosci,* 45**,** 245-57.

Giber, K., Diana, M. A., Plattner, V. M., Dugue, G. P., Bokor, H., Rousseau, C. V., Magloczky, Z., Havas, L., Hangya, B., Wildner, H., Zeilhofer, H. U., Dieudonne, S. & Acsady, L. 2015. A subcortical inhibitory signal for behavioral arrest in the thalamus. *Nat Neurosci,* 18**,** 562-8.

Glangetas, C., Girard, D., Groc, L., Marsicano, G., Chaouloff, F. & Georges, F. 2013. Stress switches cannabinoid type-1 (CB1) receptor-dependent plasticity from LTD to LTP in the bed nucleus of the stria terminalis. *J Neurosci,* 33**,** 19657-63.

Otsu, Y., Marcaggi, P., Feltz, A., Isope, P., Kollo, M., Nusser, Z., Mathieu, B., Kano, M., Tsujita, M., Sakimura, K. & Dieudonné, S. 2014. Activity-dependent gating of calcium spikes by A-type K+ channels controls climbing fiber signaling in Purkinje cell dendrites. *Neuron,* 84**,** 137-51.

Rousseau, C. V., Dugue, G. P., Dumoulin, A., Mugnaini, E., Dieudonne, S. & Diana, M. A. 2012. Mixed inhibitory synaptic balance correlates with glutamatergic synaptic phenotype in cerebellar unipolar brush cells. *J Neurosci,* 32**,** 4632-44.

Scofield, M. D., Boger, H. A., Smith, R. J., Li, H., Haydon, P. G. & Kalivas, P. W. 2015. Gq-DREADD Selectively Initiates Glial Glutamate Release and Inhibits Cue-induced Cocaine Seeking. *Biol Psychiatry,* 78**,** 441-51.

Vergnano, A. M., Rebola, N., Savtchenko, L. P., Pinheiro, P. S., Casado, M., Kieffer, B. L., Rusakov, D. A., Mulle, C. & Paoletti, P. 2014. Zinc dynamics and action at excitatory synapses. *Neuron,* 82**,** 1101-14.

Wang, H., Peca, J., Matsuzaki, M., Matsuzaki, K., Noguchi, J., Qiu, L., Wang, D., Zhang, F., Boyden, E., Deisseroth, K., Kasai, H., Hall, W. C., Feng, G. & Augustine, G. J. 2007. High-speed mapping of synaptic connectivity using photostimulation in Channelrhodopsin-2 transgenic mice. *Proc Natl Acad Sci U S A,* 104**,** 8143-8.